






The Relative Prevalence of Wave Packets and Coherent Structures in the Inertial and Kinetic Ranges of Turbulence as Seen by Solar Orbiter

Alina Bendt¹ , Sandra Chapman^{1,2,3} , and Thierry Dudok de Wit^{2,4} 
¹ Centre for Fusion, Space and Astrophysics, Physics Department, University of Warwick, UK
² International Space Science Institute, Bern, Switzerland
³ Department of Mathematics and Statistics, University of Tromsø, Norway
⁴ University of Orléans, France

Received 2024 March 4; revised 2024 May 21; accepted 2024 May 31; published 2024 August 16

Abstract

The Solar Orbiter (SO) mission provides the opportunity to study the evolution of solar wind turbulence. We use SO observations of nine extended intervals of homogeneous turbulence to determine when turbulent magnetic field fluctuations may be characterized as: (i) wave packets and (ii) coherent structures (CSs). We perform the first systematic scale-by-scale decomposition of the magnetic field using two wavelets known to resolve wave packets and discontinuities, the Daubechies 10 (Db10) and Haar, respectively. The probability distribution functions (PDFs) of turbulent fluctuations on small scales exhibit stretched tails, becoming Gaussian at the outer scale of the cascade. Using quantile–quantile plots, we directly compare the wavelet fluctuations PDFs, revealing three distinct regimes of behavior. Deep within the inertial range (IR) both decompositions give essentially the same fluctuation PDFs. Deep within the kinetic range (KR) the PDFs are distinct as the Haar decompositions have larger variance and more extended tails. On intermediate scales, spanning the IR–KR break, the PDF is composed of two populations: a core of common functional form containing $\sim 97\%$ of fluctuations, and tails that are more extended for the Haar decompositions than the Db10 decompositions. This establishes a crossover between wave-packet (core) and CS (tail) phenomenology in the IR and KR, respectively. The range of scales where the PDFs are two-component is narrow at 0.9 au (4–16 s) and broader (0.5–8 s) at 0.4 au. As CS and wave–wave interactions are both candidates to mediate the turbulent cascade, these results offer new insights into the distinct physics of the IR and KR.

Unified Astronomy Thesaurus concepts: [Solar wind \(1534\)](#); [Interplanetary turbulence \(830\)](#); [Heliosphere \(711\)](#); [Wavelet analysis \(1918\)](#); [Time series analysis \(1916\)](#)

1. Introduction

The super Alfvénic, high Reynolds number solar wind flow provides a large-scale natural laboratory for plasma turbulence (see, e.g., Tu & Marsch 1995; Bruno & Carbone 2013; Chen 2016; Marino & Sorriso-Valvo 2023). There are extensive observations at 1 au (e.g., from ACE, WIND, and Cluster) principally around the *L1* point upstream of Earth (for a review, see, e.g., Bruno & Carbone 2013; Verscharen et al. 2019). Previous observations at different distances from the Sun have been provided by, e.g., Helios, Ulysses, and Voyager (see, e.g., Bruno & Carbone 2013; Nicol et al. 2008; Cuesta et al. 2022; Yordanova et al. 2009; Bourouaine et al. 2012; Maruca et al. 2023; Pagel & Balogh 2003; Bavassano et al. 1982; Tu et al. 1984; Roberts 1990). Solar Orbiter (Müller et al. 2013, 2020) and Parker Solar Probe offer new opportunities to study the solar wind at different distances from the Sun from 1 au to within 0.1 au.

Results around 1 au consistently show features of turbulence phenomenology. The power spectrum of magnetic field fluctuations in the trace and components exhibits a well-defined inertial range (IR) of magneto-hydrodynamic (MHD) turbulence with a steeper kinetic range (KR) scaling below ion scales and a shallower, approximately $1/f$ range at larger scales (e.g., Kiyani et al. 2015). The IR trace power spectrum typically exhibits a

power spectral scaling of around $-5/3$ (e.g., Matthaeus & Goldstein 1982; Beresnyak 2012; Podesta et al. 2007), which corresponds to the Kolmogorov 1941 (K41) scaling (Kolmogorov et al. 1991). Closer to the Sun, at distances smaller than 0.4 au (e.g., Chen et al. 2020; Šafránková et al. 2023; Lotz et al. 2023) the power spectrum on average evolves toward a spectral slope of $-3/2$, which corresponds to Iroshnikov–Kraichnan (IK) scaling (Iroshnikov 1963). Below ion kinetic scales the spectrum steepens to a well-defined kinetic range (e.g., Sahraoui et al. 2009; Chen et al. 2014; Verscharen et al. 2019; Kiyani et al. 2013). The steeper kinetic range power spectrum corresponds to an increase in compressibility (Kiyani et al. 2009, 2013; Alexandrova et al. 2008, 2013) compared to the IR.

Both waves and coherent structures are features of MHD turbulent phenomenology (Tu & Marsch 1995; Frisch 1995) and may mediate the turbulent cascade. In the following, a coherent structure is a sudden discontinuity that stands out of the fluctuations. Recent studies of the KR reveal whistler waves, ion-cyclotron waves, and kinetic Alfvén waves, as well as coherent structures in this regime (e.g., Sahraoui et al. 2009; He et al. 2012; Osman et al. 2012a; Salem et al. 2012; Alexandrova et al. 2013; Wu et al. 2013; Roberts et al. 2017; Chhiber et al. 2021; Zhou et al. 2023), where kinetic effects and ultimately dissipation become important (e.g., Kiyani et al. 2015; Verscharen et al. 2019). A feature of turbulence, is intermittency, which has been identified by Koga et al. (2007) as arising from phase correlation among different scales due to nonlinear wave–wave interactions and as coherent structures by Gomes et al. (2023), Camussi & Guj (1997), and Veltri (1999).



Original content from this work may be used under the terms of the [Creative Commons Attribution 4.0 licence](#). Any further distribution of this work must maintain attribution to the author(s) and the title of the work, journal citation and DOI.

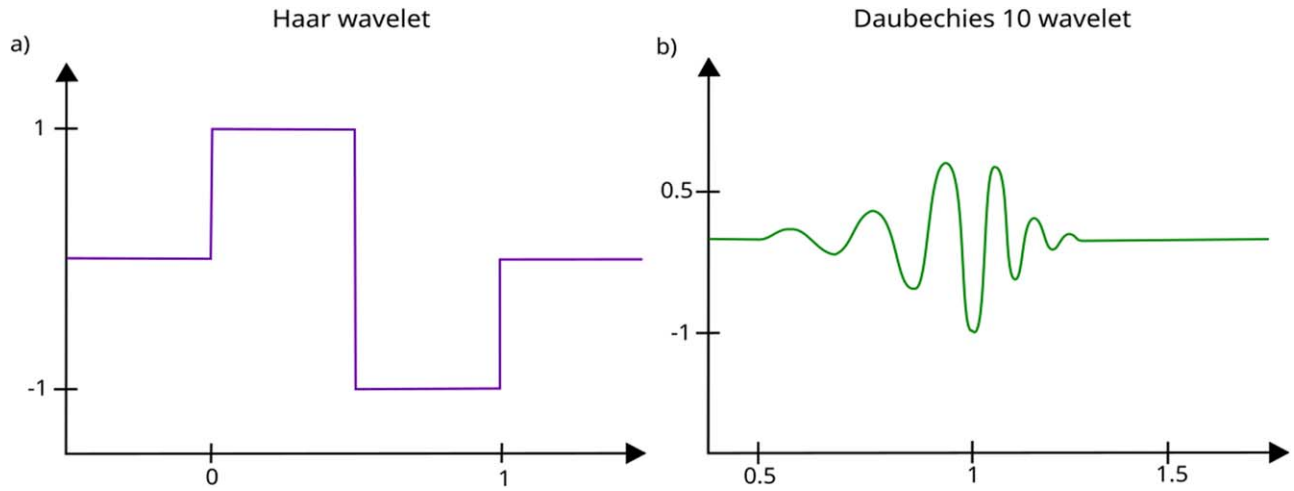


Figure 1. A schematic drawing of the Haar wavelet (a) and 10th order Daubechies wavelet (b) as functions of time.

These coherent structures have also been identified as localized sites of turbulent dissipation (Perri et al. 2012; Greco et al. 2017; Wu et al. 2013; Osman et al. 2012a, 2014, 2012b; Sioulas et al. 2022a).

Identification of turbulence rests upon statistical characterization, since quantitative aspects of turbulence are reproducible in a statistical sense and each realization is distinct (Frisch 1995; Tu & Marsch 1995). A key characteristic of turbulence is scale-by-scale similarity (Frisch 1995; Tu & Marsch 1995). The process of statistical characterization and testing for scaling includes a two-step process: (i) obtain the fluctuation time-series decomposition, by differencing, Fourier (Welch 1967), or wavelet decomposition (Farge 1991; Meneveau 1991; Daubechies 1990; Mallat 1989), followed by (ii) analyze the fluctuations scale by scale by examining power spectra and probability distribution functions (PDFs). All the above methods are in widespread use in the study of solar wind turbulence (e.g., Podesta et al. 2007; Kiyani et al. 2013; Camussi & Guj 1997; Farge 1992; Yamada & Ohkitani 1991a; Do-Khac et al. 1994; Narasimha 2007; Bolzan et al. 2009; Beresnyak 2012; Bruno & Carbone 2013; Chapman & Hnat 2007; Katul et al. 2001).

Turbulent fluctuations in solar wind data extracted by differencing the time series have non-Gaussian PDFs (Bruno & Carbone 2013; Frisch 1995; Tu & Marsch 1995; Alexandrova et al. 2008; Bruno et al. 2004, 2003; Sorriso-Valvo et al. 1999; Hnat et al. 2003) that tend to become more Gaussian on scales approaching the outer scale of the turbulent cascade. The stretched exponential tails of the PDFs (Hnat et al. 2003), hereafter referred to as stretched tails, show that large fluctuations have a higher probability of occurrence than for a Gaussian distribution, consistent with intermittency (Bruno 2019 and references therein).

In this paper, we use wavelet decompositions and perform the first systematic comparison of different features in magnetic field records by considering two types of mother wavelets: (i) Haar or first-order Daubechies wavelets are well suited for capturing sharp discontinuities (hereafter called coherent structures) such as the signature of current sheets, while (ii) 10th order Daubechies wavelets have a wave-like shape, and therefore are better adapted for detecting wave packets; see Figure 1. By comparing the two wavelet decompositions we should then be able to distinguish the role of these different features at different scales of the turbulent cascade. Different

time-series decompositions extract different features in the time series (Schneider & Farge 2001; Farge 1991, 1992). We will see that comparing different decompositions of the time series can identify how coherent structures and wave-wave interactions contribute to the turbulent cascade.

The IR of solar wind turbulence is anisotropic due to the presence of a background magnetic field (Matthaeus et al. 1990) as seen in the power spectrum (e.g., Horbury et al. 2008; Wicks et al. 2010; Chen et al. 2011; Bruno & Carbone 2013; Oughton et al. 2015; Bandyopadhyay & McComas 2021). The background field that is expected to order the anisotropy of the magnetic fluctuations can be defined globally, averaging across scales and time, or locally, scale by scale and varying in time (e.g., Yamada & Ohkitani 1991b; Horbury et al. 2008; Beresnyak 2012; Chapman & Hnat 2007; Duan et al. 2021; Kiyani et al. 2013; Podesta 2009; Turner et al. 2012; Zhang et al. 2022). These analyses can yield a broad spread in values of the power spectral exponent (Tessein et al. 2009) and differing estimates of its anisotropy (Oughton et al. 2015). In this paper we will consider the former, global background field. Averaging the magnetic field vector over a global timescale exceeding that of the center scale of the turbulence defines a global background field. Together with the time-averaged solar wind velocity, a coordinate system is constructed. The time average is typically taken over the entire intervals of data (in this study we use intervals from 10 to 31.5 hr length; Bruno & Carbone 2013).

In this paper we will find that the IR–KR transition can, depending upon conditions, coincide with the crossover to a region where coherent structures dominate the population of large fluctuations. By comparing different decompositions of the time series in a global background field, we find that coherent structures are prevalent in the KR and less dominant in the IR. The temporal scale where the power spectral density (PSD) steepens from the IR to the KR is indicative of a transition from MHD to ion kinetic physics. There has been considerable effort to identify this scale break, and it does not necessarily appear at the same scale for any plasma conditions (Markovskii et al. 2008; Chen et al. 2014; Wang et al. 2018; Šafránková et al. 2023). Generally, the spectral break occurs between 0.02 and 4 Hz (Markovskii et al. 2008). Recently, Šafránková et al. (2023) found that the spectral break decreases

Table 1
The Nine Interval Characteristics

Interval (Y-M-D)	length (hr)	R (au)	V_{sw} (km s ⁻¹)	τ_{adv} (hr)	β	ρ_i (Hz)	KR break (Hz)	θ (deg)
2022-01-01	~14	0.997	584	70.96	1.36	0.31	0.5	27.14
2022-01-03	~15.3	0.992	530	77.68	1.55	0.19	0.5	31.82
2022-01-04	~10.75	0.989	438	93.87	0.95	0.24	0.25	18.07
2022-01-06	~24	0.984	312	130.94	1.79	0.23	0.5	64.51
2021-11-18	~14.75	0.934	533	72.82	2.08	0.19	1	160.93
<i>2023-03-14</i>	~10	0.597	548	45.27	2.48	0.68	1	68.63
<u>2022-03-18</u>	~12	0.369	414	37.08	0.98	1.35	1	7.29
<u>2022-04-04</u>	~24	0.369	555	27.64	0.76	1.22	1	16.82
<u>2022-04-01</u>	~31.5	0.344	535	26.66	1.02	1.75	1	21.46

Note. Columns show the date, length, heliocentric distance R , average solar wind speed V_{sw} , advection times τ_{adv} , plasma β , ion-gyro frequency ρ_i , the KR–IR spectral break timescale, and the field alignment angle θ . R is quoted to three significant figures to distinguish intervals very close to each other, while the other parameters (except V_{sw}) are quoted to two decimal places. The spectral break scale is quoted for the perpendicular field components.

with heliocentric distance from around 4 Hz close to the Sun to 0.1 Hz around 1 au.

This paper is organized in three sections. In Section 2 we present the data intervals analyzed and data analysis methods. In Section 3 we present a systematic comparison of power spectra and fluctuation PDFs applied to two different scale-by-scale decompositions of the data. We conclude in Section 4.

2. Data and Methods

2.1. Data

We analyze in detail the time series of magnetic field data from the Magnetometer (MAG; Horbury et al. 2020) and obtain averaged parameters from the solar wind velocity, density, pressure, and temperature measurements of the Solar Wind Analyser (SWA-PAS; Owen et al. 2020) on board Solar Orbiter (Müller et al. 2013). The solar wind velocity and magnetic field measurements are provided in *RTN* coordinates, with the magnetic field measurements at a cadence of 8 Hz. We select nine over 10 hr long intervals of turbulence that contain homogeneous solar wind flow without any shocks, current sheet crossings, and other large events, at heliocentric distances R of ~ 0.3 , 0.6, and ~ 0.9 au. Three intervals have a plasma $\beta \geq 1.7$. The average solar wind velocity of the intervals, V_{sw} , is 494 km s⁻¹. Table 1 presents the intervals, grouped in four categories: (i) the high plasma beta of $\beta \geq 2$ intervals from 2021 November 18 at 0.9 au and 2023 March 14 at 0.6 au (italics); (ii) this encompasses the interval with a large field alignment angle θ (bold); (iii) intervals close to the Sun (underlined); and (iv) intervals at ~ 0.9 au with moderate plasma β (no underline). We rotate the magnetic field from *RTN* coordinates into coordinates ordered by the global time-averaged background field, averaged over the entire interval B_0 . The orthogonal coordinate system then has the magnetic field projected onto a component B_{\parallel} parallel to B_0 , and onto perpendicular components $B_{\perp(V_{sw}, B)} = B_{\parallel} \times V_{sw}$ and $B_{\perp(V_{sw} \times B)} = B_{\parallel} \times B_{\perp(V_{sw}, B)}$.

2.2. Wavelet Decompositions of the Time Series and Intermittency Measures

We decompose the magnetic field time series of these nine intervals of homogeneous turbulence using two different discrete wavelet transforms, the 10th order Daubechies (Db10) and Haar wavelet (the latter is equivalent to differencing of the time series). The different wavelets are designed to

resolve wave-like features and sharp changes in the time series, respectively (Daubechies 1990; Farge 1992; Torrence & Compo 1998; Percival & Walden 2000). A schematic drawing of the shape of the Haar and Db10 wavelets are presented in Figure 1.

Fourier or wavelet decompositions, and differencing (structure functions) have all been used extensively in the study of solar wind turbulence, especially in testing for statistical scaling (e.g., Yamada & Ohkitani 1991a; Farge 1992; Do-Khac et al. 1994; Katul et al. 2001; Chapman & Hnat 2007; Narasimha 2007; Podesta et al. 2007; Bolzan et al. 2009; Kiyani et al. 2013). Wavelet decompositions are time-frequency localized and therefore are well suited to isolating wave packets and coherent structures (Daubechies 1990; Farge et al. 1996). The discrete wavelet transform decomposes the time series into two components: a low passband, known as the approximation, and a high passband, known as the detail. The procedure is applied iteratively to the approximations, which are on successively longer timescales. The cutoff frequencies define a dyadic sequence (Farge 1992; Percival & Walden 2000) so that the set of wavelet details are the time-series bandpass filtered around central frequencies and bands of widths $2^j \Delta$, where Δ is the sampling period.

We will use τ to denote the scale of decomposition and t_k as discrete time for the magnetic field time series denoted as $B(t)$. The wavelet details $\delta B_{\tau, t_k}$ at a timescale $\tau = 2^j \Delta$, where Δ is the sampling period, $j \in \mathbb{Z}$ the scale, and t_k the location of the magnetic field $B(t)$, are (Farge et al. 1996)

$$\delta B_{\tau, t_j} = \sum_{k=1}^N B(t_k) \sqrt{\tau} \Psi(t_k - t_j), \quad (1)$$

where N is the length of the data set and $\Psi_{j,i}$ is the set of wavelets. The power spectrum can then be defined as (Farge 1992; Schneider & Farge 2001)

$$E(t', \tau) = \frac{2\Delta}{N} |\delta B_{\tau, t_j}|^2. \quad (2)$$

Wavelet transforms thus sample the frequency space logarithmically, which is well suited to the determination of the power-law exponent of the power spectrum (Mallat 1989). The Haar wavelet is a first-order Daubechies wavelet. The Daubechies family is defined from the base wavelet:

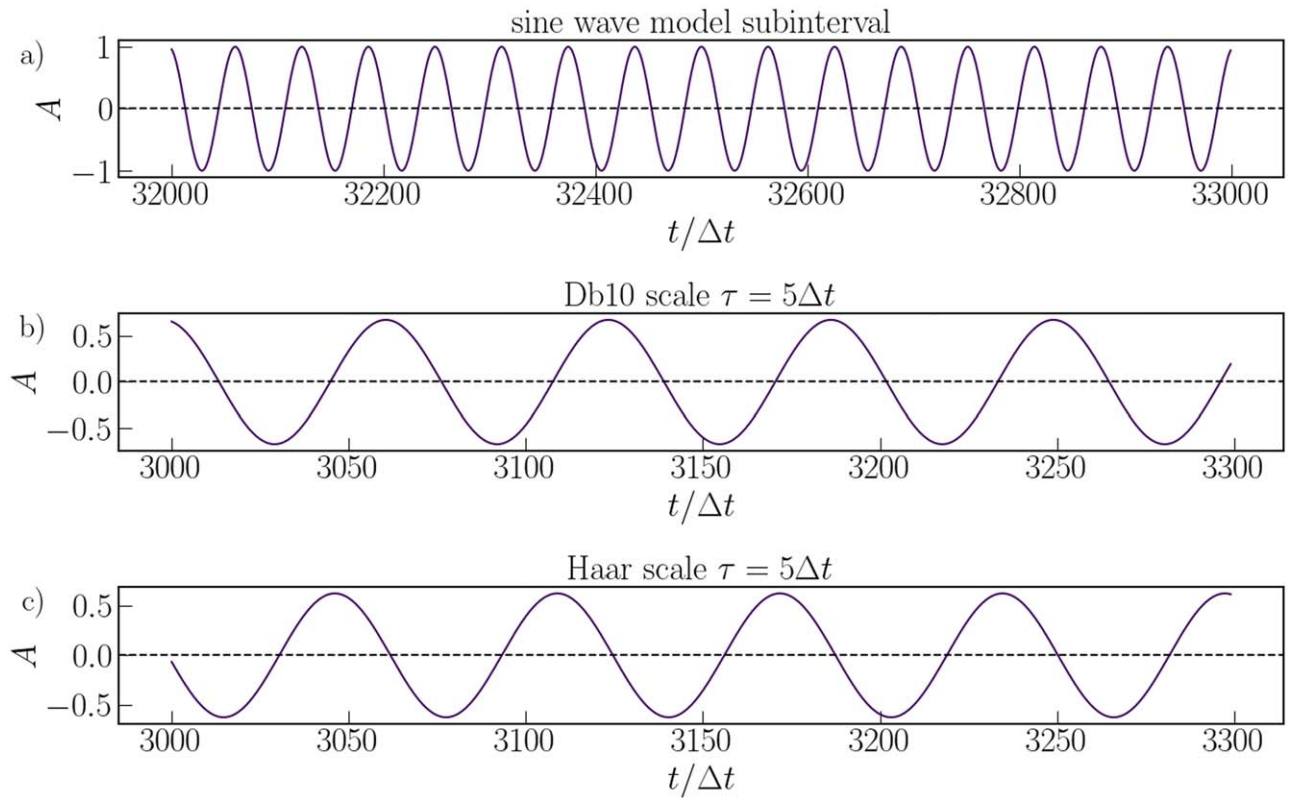


Figure 2. Wavelet decomposition of a sine wave model at scale $\tau = 5\Delta t$ (a) using the Db10 wavelet (b) and the Haar wavelet (c). Both wavelet decompositions produce a sine wave with the same amplitude.

(Nickolas 2017)

$$\Psi(x) = \sum_{k=0}^{2N-1} (-1)^{k-1} a_k \Phi(2x + k - 1) \quad (3)$$

and the scaling function Φ :

$$\Phi(x) = \sum_{k=0}^{2N-1} a_k \Phi(2x - k) \quad (4)$$

where the coefficients a_k have to satisfy several conditions, and $k \in \mathbb{Z}$ and $N \in \mathbb{N}$. The construction of the Daubechies family of wavelets can be found in Nickolas (2017). The Haar wavelet H is a step-function $H_{j,k}(x) = 2^{j/2} H(2^j x - k)$ (Nickolas 2017). Since the Haar wavelet shape corresponds to sharp changes it will be sensitive to coherent structures. The 10th order Daubechies wavelet (Db10) is determined from a base wavelet with 10 wavelet coefficients (Daubechies 1992; Percival & Walden 2000), and its shape corresponds to that of wave packets. The Db10 wavelet has a higher number of vanishing moments than the Haar wavelet, enabling a more accurate determination of steeper power-law exponents in the kinetic range (Farge et al. 1996). Power spectral estimates rely upon an accurate estimation of the total power in each discrete frequency band, which can be distributed linearly (Fourier), or in steps of 2^k (wavelets). The fidelity of the power spectrum will depend upon the method used to obtain the time series in each frequency band. It has been shown previously that for spectra steeper than -3 the Haar wavelet does not produce converging estimates for the power in each frequency band (Cho & Lazarian 2009) and, therefore, cannot be used to

estimate the spectral scaling steeper than -3 . For that reason the wavelet transform with Haar mother wavelets should be interpreted with great care in the KR. However, both the Haar and Db10 wavelet decompositions are well-defined methods to resolve fluctuations on different temporal scales from a time series (Nickolas 2017; Percival & Walden 2000). The Haar wavelet performs a differencing that is similar (Lovejoy & Schertzer 2012) to that used in the well-known structure function defined as $S_q(\tau) = \langle |\delta B(\tau, t_j)|^q \rangle_t \sim \tau^{\zeta(q)}$, which is at the core of analysis of turbulent fields (Frisch 1995; Tu & Marsch 1995). Therefore, we use both Haar and Db10 wavelet decompositions to study the fluctuation PDFs and how they vary with temporal scale. The wavelet transform is performed by the Maximum Overlap Discrete Wavelet Transform (MODWT; Hess-Nielsen & Wickerhauser 1996; Percival & Walden 2000) with reflected boundaries.

A simple illustration of the different performance of the Haar and Db10 wavelet decompositions is provided in Figures 2 and 3. The wavelet decompositions are applied to a sine wave (Figure 2) and a random spike train (Figure 3). The two wavelet decompositions perform similarly on the sine wave; in both cases a sinusoid of similar amplitude is resolved. The phase shift between panels (b) and (c) of Figure 2 is due to the different time asymmetry properties of the wavelets. For the random spike train, the two wavelet decompositions yield quite distinct time series: the Haar wavelet decomposition more closely reflects the time structure of the original time series and is about an order of magnitude larger in amplitude than the Db10 wavelet decomposition time series. Comparing these two decompositions, and in particular the PDF of their coefficients,

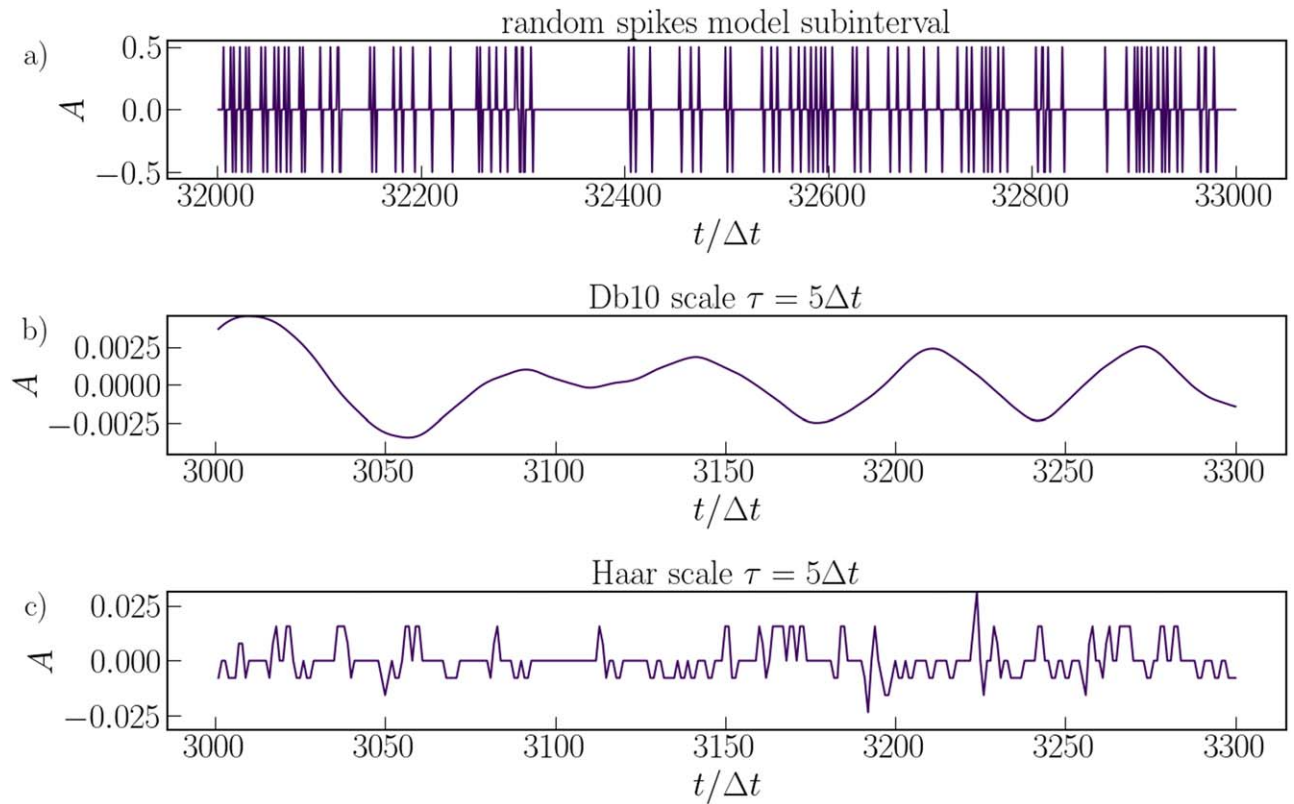


Figure 3. Wavelet decomposition of a random spike model at scale $\tau = 5\Delta t$ (a) using the Db10 wavelet (b) and the Haar wavelet (c). The Haar wavelet decomposition (c) more closely reflects the fine structure of the original time series compared to the Db10 wavelet decomposition (b). The Haar wavelet decomposition amplitude is approximately one order of magnitude larger than the Db10 wavelet decomposition amplitude.

we can then discriminate between time series that contain a predominance of sharp discontinuities (i.e., coherent structures) and wave packets. Case (i) will yield fluctuations of similar amplitude, whereas case (ii) will yield Haar wavelet decomposed fluctuations of significantly larger amplitude than fluctuations obtained by the Db10 wavelet decomposition.

3. Results

We obtain scale-by-scale decompositions of the nine intervals using both Haar and Db10 wavelets, which then provide estimates of the power spectra and the fluctuation PDFs and their moments scale by scale. The aim is twofold: (i) to verify that the selected intervals do indeed exhibit properties consistent with turbulence phenomenology; and (ii), by comparing the results of these analyses for the Haar (that is, time-series differences) and the Db10 wavelets, to gain new insights into the relative importance of coherent structures and wave-like features at different temporal scales across the turbulent cascade.

3.1. Power Spectra

We first establish that the power spectral estimates (Figure 4) of the Haar and Db10 discrete wavelets show a clearly defined inertial range with power spectral breaks at low frequencies to the $1/f$ range and at high frequencies to the kinetic range, consistent with a well-developed turbulence cascade. Figure 4 presents the power spectral density (PSD) for a representative interval for all magnetic field components, (a) $B_{\perp(V_{sw},B)}$, (b) $B_{\perp(V_{sw},B)}$, and (c) B_{\parallel} . The full set of PSDs for all intervals is presented in Figure A3. Each spectrum is a single estimate using the full temporal range of each interval and is not

averaged. The parallel magnetic field component consistently shows less power than the perpendicular components (e.g., Šafránková et al. 2023). The intervals closer to the Sun overall show more power at all scales (Figure A4 presents the standard deviation of the wavelet fluctuations for all intervals), as previously observed by Chen et al. (2020). The spectral exponents generally do not present clear IK or K41 scaling but rather values that lie between those values, as also seen by Wang et al. (2023).

As expected, the Haar and Db10 wavelet estimates diverge in the KR, seen in Figure 4, as the Haar cannot resolve scaling exponents steeper than -3 (Cho & Lazarian 2009). Therefore, the Haar wavelet cannot reliably identify the scaling exponent in the KR; however, it does provide appropriate fluctuations from the decomposition. However, both the Haar and Db10 spectral estimates, within their given frequency resolution, identify the same location of the spectral break, which is identified as the smallest scale at which the wavelet PSDs coincide. The IR–KR spectral break scale moves with the larger of the ion scales ρ_i and d_i (blue vertical lines in Figure 4, which are reproduced for all intervals in Figure A3), decreasing with decreasing distance from 4 to 1 s and plasma $\beta \geq 2$. The evolution of the spectral break was previously observed by Šafránková et al. (2023), Lotz et al. (2023), and Bruno & Trenchi (2014) for magnetic field trace spectra. For B_{\parallel} the spectral break differs by one dyadic scale to the perpendicular components for $\beta \geq 2$ and the interval 2022 January 3 at 0.992 au.

The outer inertial range spectral break to the $1/f$ range (Figure 4) is typically located before the 1 hr scale. The early $1/f$ break is most evident in B_{\parallel} and $B_{\perp(V_{sw},B)}$. The break between the IR and $1/f$ is well resolved in our wavelet spectral

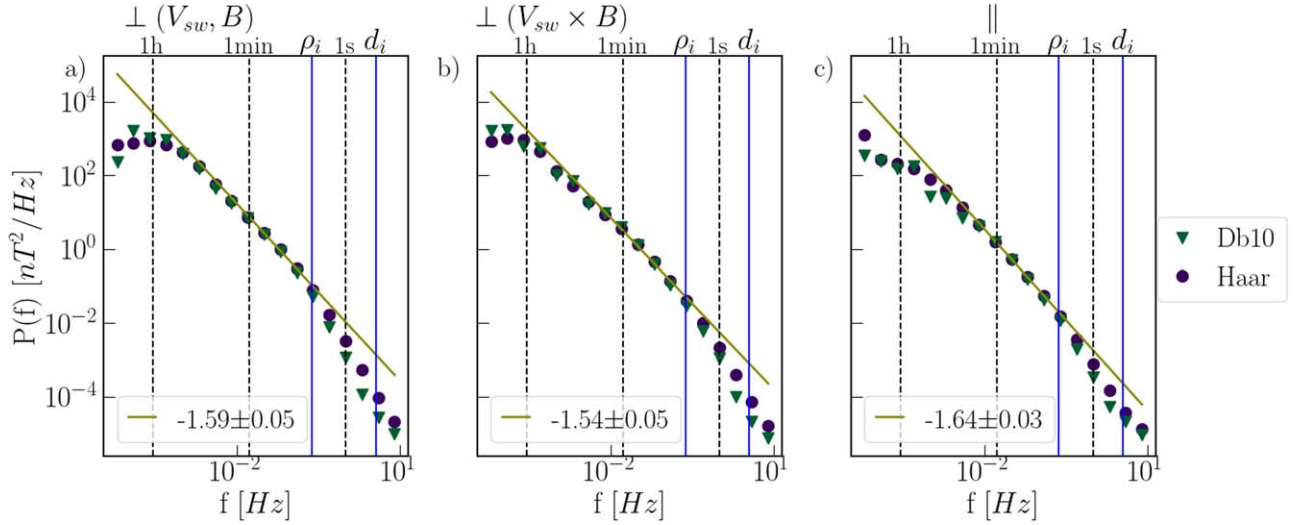


Figure 4. PSD with clear $1/f$, inertial, and kinetic ranges in both Haar and Db10 wavelet decompositions. PSDs are shown for one representative interval for each magnetic field component (column) and the respective scaling exponent in the inertial range fitted on the Haar wavelet decompositions. The interval is at 0.989 au with $\beta = 0.95$ and $\theta = 18^\circ 07$ from 2022 January 4. The Db10 wavelet decomposition is shown by green triangles; purple circles are the Haar wavelet decomposition. Blue vertical lines denote the ion-gyro frequency ρ_i and ion-inertia length d_i . Dashed black vertical lines denote scales marked on the x-axis as 1 s, 2 s, 1 minutes, and 1 hr. Yellow fit lines to the Haar wavelet power spectrum show the spectral exponent, which is quoted to three significant figures.

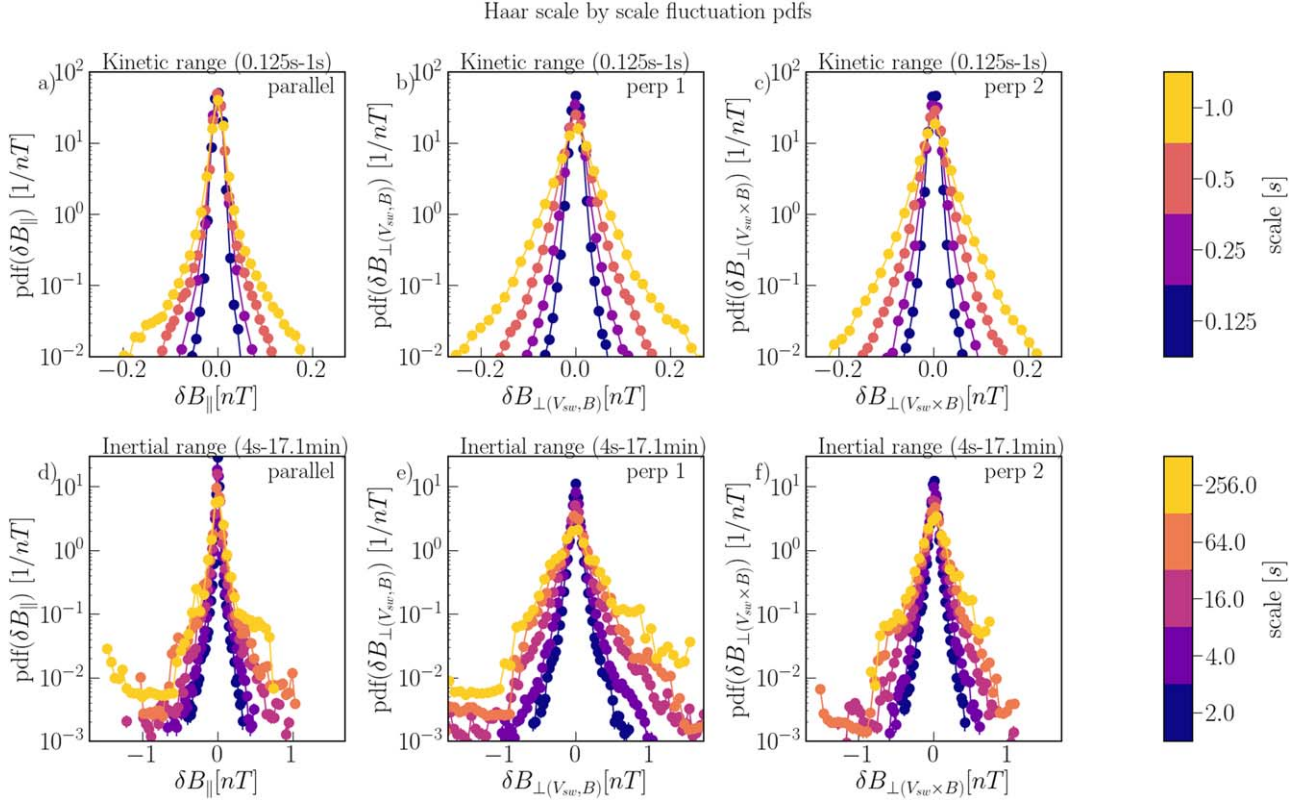


Figure 5. PDFs of Haar wavelet decompositions developing from stretched-tailed KR PDFs to Gaussian-like outer-scale PDFs. PDFs are shown for each component (columns) of the magnetic field for the KR (top row, panels (a) to (c)) up to 1 s and IR (bottom row, panels (d) to (f)) for the interval at 0.989 au from 2022 January 4. The color marks the scale, with largest scale in yellow and smallest scale in blue. The PDFs are normalized by bin width and overall number of samples of magnetic field data. The number of bins is scaled by the standard deviation σ at the corresponding scale, and bins with fewer than 10 counts are discarded. The error is estimated as \sqrt{n} , where n is the bin count; error bars are too small to be resolved visually.

estimates, which do not require multisample averaging; the break frequency decreases with decreasing distance. This was also reported by Chen et al. (2020), who averaged each interval over sliding window Fourier magnetic field trace spectra to obtain the break at $\sim 10^4$ s for large and $\sim 10^3$ s for small distances from the Sun.

3.2. Fluctuation PDFs Scale by Scale

Turbulence is routinely studied by decomposing the observed time series into fluctuations on different temporal scales. Here, we compare the fluctuation PDFs extracted by the Haar (comparable to differencing) and Db10 wavelets (which

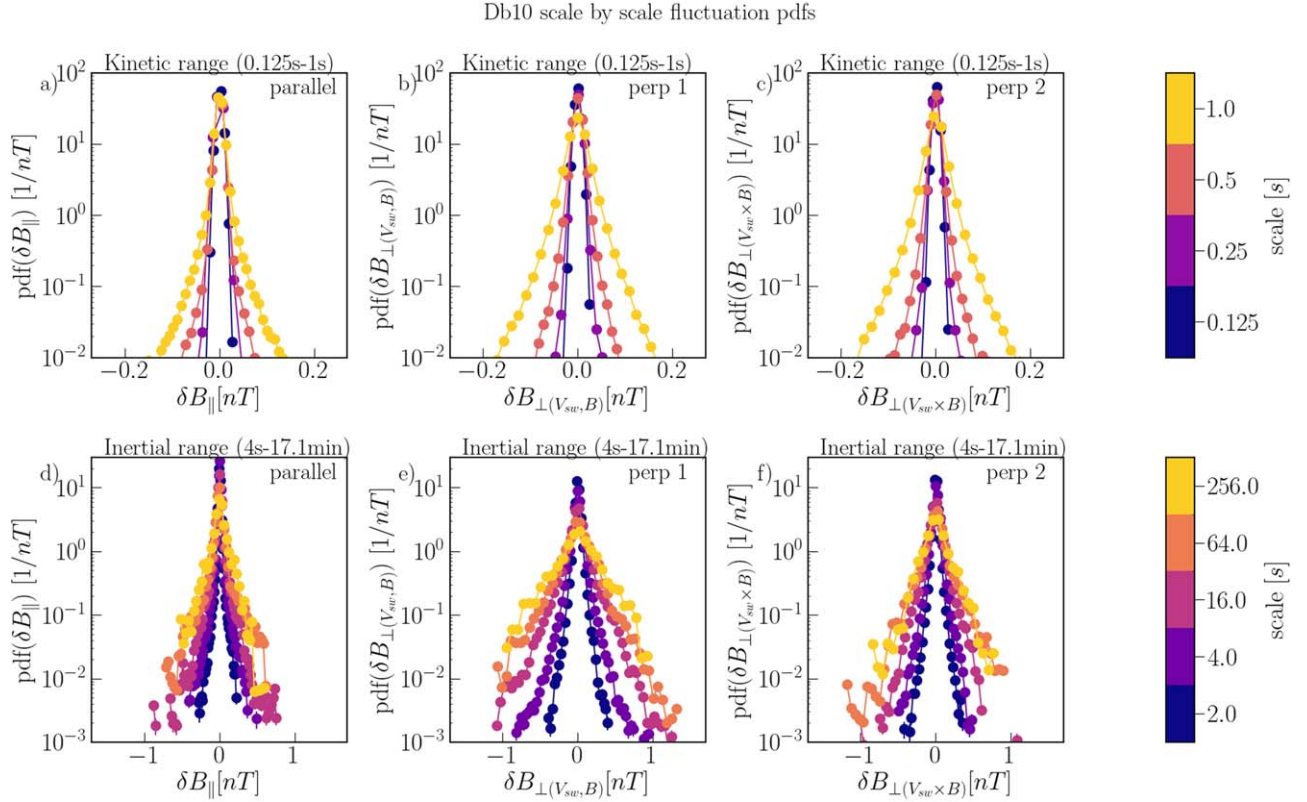


Figure 6. PDFs of Db10 wavelet decompositions developing from stretched-tailed KR PDFs to Gaussian-like outer-scale PDFs. PDFs are shown for each component (columns) of the magnetic field for the KR (top row, panels (a) to (c)) up to 1 s and IR (bottom row, panels (d) to (f)) for the interval at 0.989 au from 2022 January 4. The color marks the scale, with largest scale in yellow and smallest scale in blue. The PDFs are normalized by bin width and overall number of samples of magnetic field data. The number of bins is scaled by the standard deviation σ at the corresponding scale, and bins with fewer than 10 counts are discarded. The error is estimated as \sqrt{n} , where n is the bin count; error bars are too small to be resolved visually.

resolve discontinuities), and wave packets, respectively, to discriminate between wave packets and coherent structures phenomenology at different scales within the turbulence cascade. As we move from the shortest to the longest scales, the fluctuation PDF evolves from a sharply peaked functional form with extended tails to Gaussian-like at the outer scale of the turbulence inertial range (Figure 5 presents the Haar wavelet decomposition PDFs and Figure 6 the Db10 wavelet PDFs; Bruno et al. 2004; Alexandrova et al. 2008; Frisch 1995; Tu & Marsch 1995). The overall amplitude of the fluctuations, captured by their standard deviation, grows with temporal scale in a manner consistent with power-law scaling in the power spectral density (Figure A4 compares the standard deviation of the wavelet fluctuation PDFs for all intervals). Specific coherent structures have been found to lie within the stretched tails of the fluctuation distributions (Bruno 2019 and references therein). Coherent structures have been identified as origins of intermittency and sites of dissipation (e.g., Osman et al. 2012a, 2012b; Greco et al. 2017; Veltri 1999; Gomes et al. 2023). This confirms that the selected intervals are exhibiting the typical characteristics of turbulent fluctuations.

In Figure 7 we directly compare the fluctuation PDFs of the two wavelet decompositions across scales spanning the KR and IR. A full set of the fluctuation PDFs of both wavelet decompositions is provided in Figures A5, A6, and A7 for each magnetic field component. Four different intervals are shown in Figure 7 (rows), where the heliocentric distance decreases from top to bottom. The scales (columns in Figure 7) shown are at 0.25, 0.5, 2, and 8 s. We find that three different morphologies

of the PDFs can be seen in Figure 7. In the KR (columns (1) and (2)), the Haar (green circles) and Db10 (purple circles) fluctuation extremes, or tails, diverge. The Haar fluctuation PDF exhibits more stretched and extended tails than the Db10 wavelet decomposition. Deep in the IR (column (4)), there is a well-defined distribution core where the Haar and Db10 extracted fluctuation PDFs coincide. This core is between the blue vertical lines (column (4)), whereas in the KR two distinct PDFs are found. On intermediate scales (column (3)), the PDFs have two components: the core of the fluctuation PDFs overlap, whereas the tails of the fluctuation PDFs diverge. The tails of the PDF obtained from the Haar wavelet decomposition are more extended than those obtained from the Db10 wavelet decomposition. The intermediate crossover range generally spans the spectral break scale obtained from the PSD. This suggests three different regimes of turbulence: (i) consistent with coherent structures in the kinetic range, (ii) consistent with wave packets deep in the inertial range, where the fluctuation PDFs overlap, and (iii) a crossover regime on intermediate scales, where a two-component PDF is observed with tails consistent with coherent structures.

The distribution functions may differ in their functional form, in their moments, or in both. We can discriminate this with compensated quantile–quantile (QQ) plots (Wilk & Gnanadesikan 1968; Easton & McCulloch 1990; Tindale & Chapman 2017) of the wavelet fluctuation PDFs (see Section A.1.1 for a description of QQ plots). If the Haar and Db10 PDFs are drawn from the same distribution, then the compensated quantile trace will be a horizontal straight line at

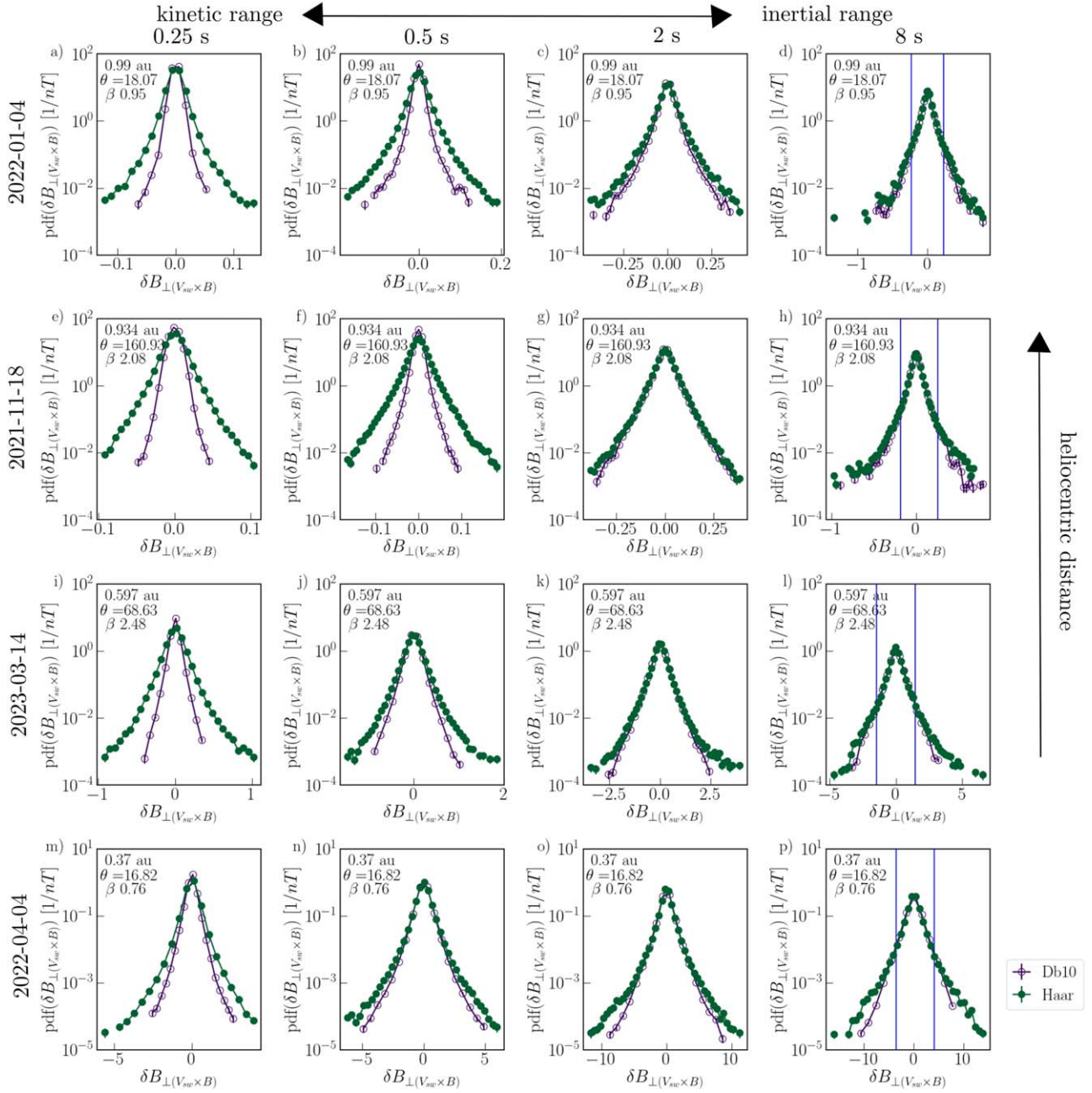


Figure 7. PDF comparison between Haar and Db10 wavelet decompositions of the magnetic field. PDFs are shown for $B_{\perp}(V_{sw} \times B)$ for four example intervals (rows). The chosen intervals (top down) are at 0.989 au with $\beta = 0.95$ and $\theta = 18.07^{\circ}$, at 0.934 au with $\beta = 2.08$ and $\theta = 160.93^{\circ}$, at 0.597 au with $\beta = 2.48$ and $\theta = 68.63^{\circ}$, and at 0.37 au with $\beta = 0.76$ and $\theta = 16.82^{\circ}$. The scales shown are increasing from left to right at 0.25, 0.5, 2, and 8 s. Empty purple circles are obtained from the Db10 wavelet decomposition, while green circles are from the Haar wavelet decomposition. The PDFs are normalized by bin width and overall number of samples of magnetic field data. The number of bins is scaled by the standard deviation σ at the corresponding scale, and bins with fewer than 10 counts are discarded. The error is estimated as \sqrt{n} , where n is the bin count; error bars are too small to be resolved visually.

zero. If the PDFs are drawn from the same functional form but with different variance, the quantile trace will be a straight line diagonally. A nonlinear relationship on the QQ plot indicates that the two distributions have different functional forms.

An example of analysis by QQ plot for these data is provided by Figure 8. The figure plots fluctuation PDFs in the KR (column (1)), IR (column (3)), and intermediate scales (column (2)). The top row of panels overlay the Haar and Db10 wavelet fluctuation PDFs, and we can see that while these coincide within the IR (panel (c)) the Haar fluctuation distribution is much broader in the KR (panel (a)). A more detailed comparison of the PDFs is afforded by QQ plots as shown in

schematic (second row) and as obtained from the data (third row). We have normalized the wavelet fluctuations by the overall magnetic field magnitude of each interval. In the KR scale (0.25 s (column (1); panel (d)) in Figure 8), the quantiles can then be seen to lie on a single line along $y = Ax$. This indicates that the Haar fluctuation PDF has a larger variance than the Db10 fluctuation PDF, but the PDFs share the same functional form. This difference in variance between the two PDFs is given by the gradient of the QQ plot trace, A . This gradient can be seen from Figure 9 to decrease with increasing temporal scale. On average, the variance obtained from the Haar fluctuation PDFs is larger than that obtained from the

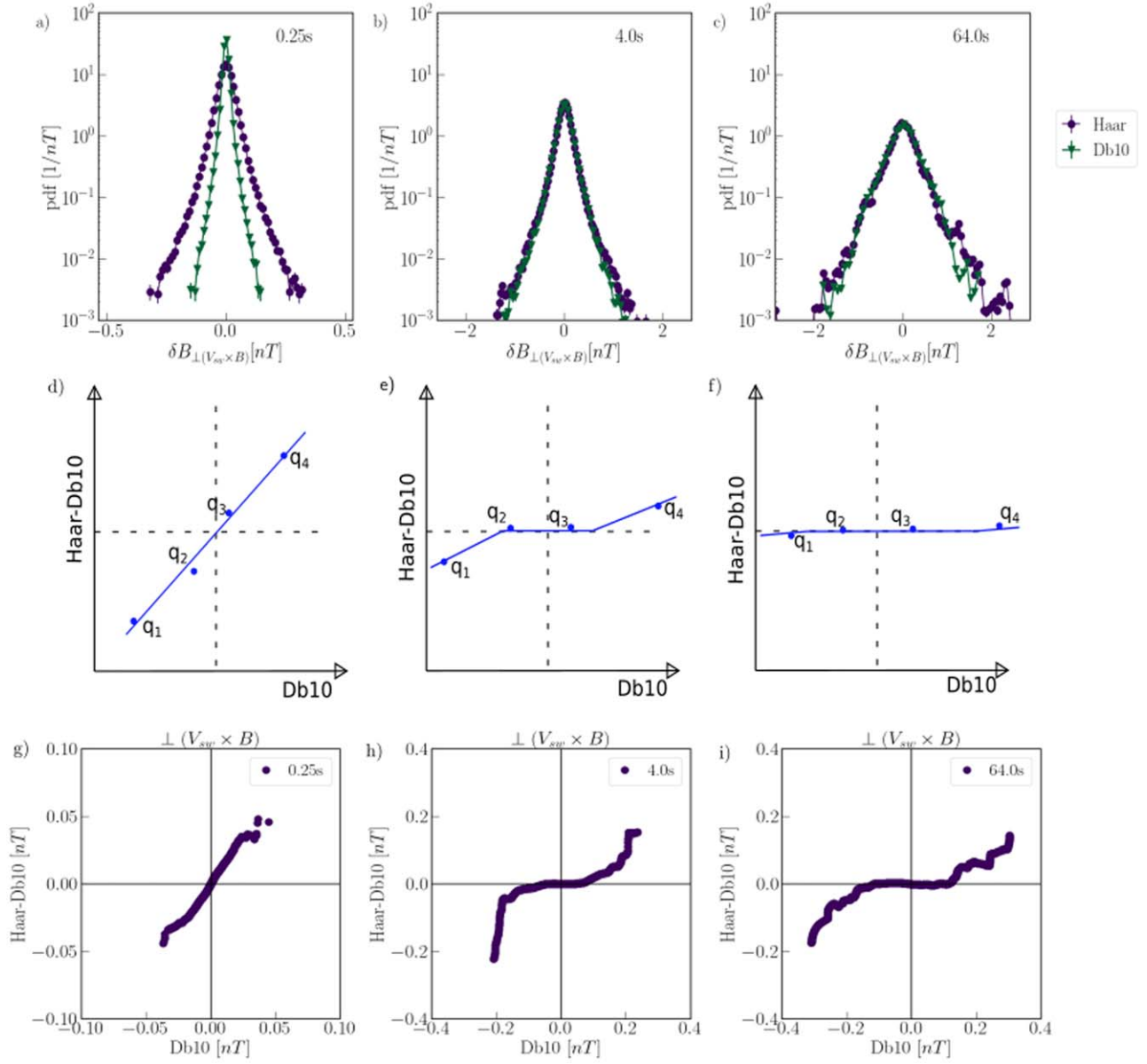


Figure 8. Compensated QQ plots compare the functional forms of the wavelet fluctuation PDFs. The compensated QQ plots are of the $H - Db10$ vs. the Db10 wavelet details for the magnetic field component $B_{\perp(V_{sw} \times B)}$. The distributions for three example scales in the three different regimes are presented with the corresponding compensated QQ plots and their schematic drawing. The interval is at 0.9 au from 2022 January 1. If the quantiles lie on the horizontal black line the distributions are the same.

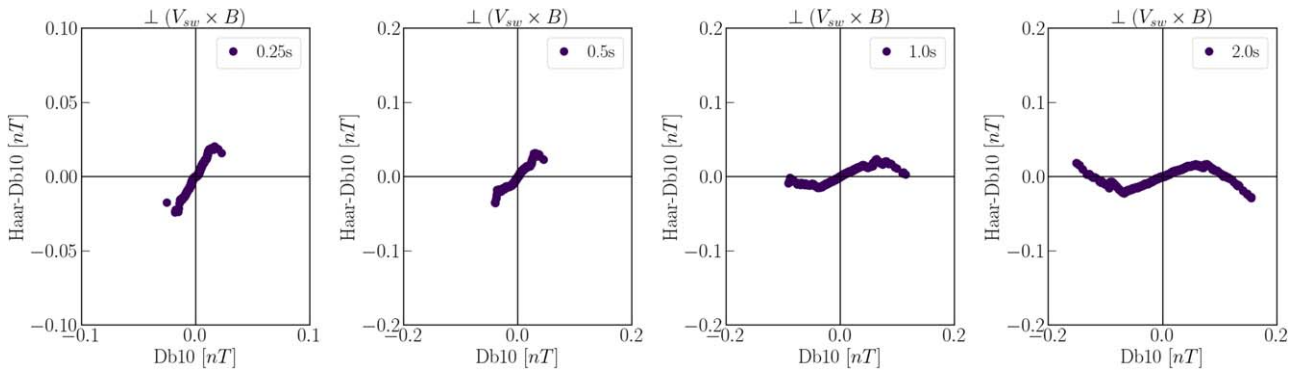


Figure 9. Compensated QQ plots compare the functional forms of the wavelet fluctuation PDFs. The compensated QQ plots are of the $H - Db10$ vs. the Db10 wavelet details for 0.25–2 s scales in the kinetic range. The interval is at 0.9 au from 2022 January 4. If the quantiles lie on the horizontal black line the distributions are the same.

Db10 fluctuation PDFs at kinetic range scales. The larger variance of the Haar fluctuation PDFs compared to the Db10 fluctuation PDFs is seen in the bottom row of Figure A4 where we present the percentage difference between Haar wavelet and Db10 wavelet estimates of the standard deviation with scale. The percentage difference is between 20% and 125% in the KR, while it is between 0% and 20% in the IR. In the IR scale in Figure 8 (4 and 64 s; columns (2) and (3)), the quantile trace has a central region that lies along $y=0$ so that the Haar and Db10 wavelet decomposition PDFs are similar in this central core. The largest fluctuations depart from this and form a distinct tail; more large fluctuations are obtained by the Haar wavelet decomposition than from the Db10 wavelet decomposition. The IR distributions are thus of a two-component character with a central core distribution, where the wavelet decompositions have the same functional form and variance, and tails of same underlying functional form with different variance where the Haar wavelet decomposition resolves larger-amplitude fluctuations. We present the compensated QQ plots for four example intervals (Figure 10, rows) at 0.9 au, at 0.9 au with $\theta = 160^\circ 93$, at 0.597 au and $\beta = 2.48$, and lastly at 0.3 au, and the magnetic field components (columns). Each color refers to the fluctuations at a given temporal scale: the largest scale in purple at 64 s and the smallest scale in teal at 0.25 s. A full set of QQ plots for all intervals is provided in Figure A8. This figure shows the evolution of the fluctuation distributions from KR morphology, through the intermediate scales with two-component character, to IR morphology. Blue vertical lines (column (3)) in Figure 10 for 8 s denote the limits of the core. These points are also marked in Figure 7 (column (4)). At 8 s about 97% of the fluctuations are within the core distribution between the blue lines. At 64 s there is a small increase to an average of 98.5%. Within this overall behavior there are differences depending on the heliocentric distance and field alignment angle θ . At 0.9 au, $\beta = 2.08$, and $\theta = 160^\circ 93$ (panels (e) to (f)), the PDF exhibits an abrupt crossover where at 1 s (the spectral break) a core appears containing 97% of the fluctuations, and the fraction of fluctuations within the core does not increase with increasing scale. This abrupt crossover is not seen for the other high β interval (panels (h) and (i)). A more comprehensive study may reveal other factors that affect the temporal scale and behavior of the crossover. For intervals $R \leq 0.4$ au a core is seen at 0.5 s containing about 92% of fluctuations in the core. The crossover range ends at 8 s for $R \leq 0.6$ au and at 16 s for $R \sim 0.9$ au. The crossover range is thus broader at small distances from the Sun than at larger distances.

The first column in Figure 10 shows the B_{\parallel} component with the KR scales consistently as single line, where the Haar wavelet fluctuation PDFs have larger-amplitude tails and with increasing scale the core expands and the amplitude of the tails of the Haar wavelet fluctuation PDF decreases. At 0.597 au and large β (row 3) the distributions show a mixture of behaviors, with $B_{\perp}(V_{sw} \times B)$ exhibiting the same evolution as intervals close to the Sun, and $B_{\perp}(V_{sw}, B)$ similar to intervals at larger distances.

In summary, given that the Haar wavelet decomposition preferentially resolves coherent structures when compared to the Db10 wavelet, these results show that the KR is dominated by coherent structures across all amplitudes of fluctuations, whereas fluctuations in the IR are two-component in character, with an extended tail dominated by coherent structures and a

core that can be consistent with either coherent structures or wave packets.

4. Conclusions

We performed a scale-by-scale analysis of the magnetic field in a coordinate system ordered by the direction of the global, time-averaged background magnetic field for each of nine intervals of solar wind turbulence seen by Solar Orbiter for different plasma parameters and solar distances. We compared time-series decompositions using the Haar (equivalent to differencing) and Db10 wavelets that distinguish discontinuities (coherent structure phenomenology), and wave packets (the phenomenology of wave-wave interactions), respectively. This work presents the first systematic comparison of these methods in the context of solar wind turbulence using wavelet decompositions that specifically characterize wave-like and coherent structure-like features in the time series. As we move from the shortest to the longest scales, the fluctuation PDF moves from a sharply peaked functional form with extended, super-exponential tails to Gaussian at the outer scale of the turbulence (Frisch 1995; Camussi & Guj 1997). The overall amplitude of the fluctuations, captured by their standard deviation, grows with temporal scale in a manner consistent with power-law scaling in the power spectral density (Figure A4). However, we find that the fluctuation PDF functional form depends upon the decomposition used to obtain the fluctuations. We directly compared the PDFs of fluctuations obtained from Haar and Db10 wavelet decompositions. We find that the fluctuation PDFs reveal three distinct morphologies.

1. Deep in the KR, the Haar and Db10 wavelet decompositions share the same functional form but the Haar wavelet decompositions have a variance that is larger than that obtained by the Db10, consistent with the phenomenology of coherent structures.
2. Deep in the IR, there is a well-defined distribution core where the Haar and Db10 wavelet decomposition PDFs coincide and have the same functional form. The core contains about 98% of fluctuations from the 64 s scale.
3. At intermediate scales between the IR and KR, the Haar wavelet decomposition forms a larger-amplitude PDF tail compared to that of the Db10 wavelet decomposition. This is consistent with fluctuations in the distribution tails being dominated by coherent structures.
4. The intermediate crossover range of scales is located around the IR-KR spectral break scale. The characteristics of this crossover range depend on heliocentric distance. At distances of around 0.9 au the crossover range is quite narrow, from 4 to 16 s. At around 0.3 au, the crossover occurs over a broader range of scales from 0.5 to 8 s.
5. For one case where the field alignment angle θ is large, $160^\circ 93$, the crossover is abrupt at 1 s compared to other cases examined here. For this case, the fluctuation PDFs derived from the Haar and Db10 wavelet decompositions do not fully coincide even at the largest scales of the IR. This suggests further work to reveal which factors affect the character and temporal scale of the crossover.

Our results highlight the multicomponent nature of the PDFs of fluctuations that can arise from either of two distinct phenomenologies that mediate the turbulent cascade, wave packets and coherent structures. We thus find that the fluctuation

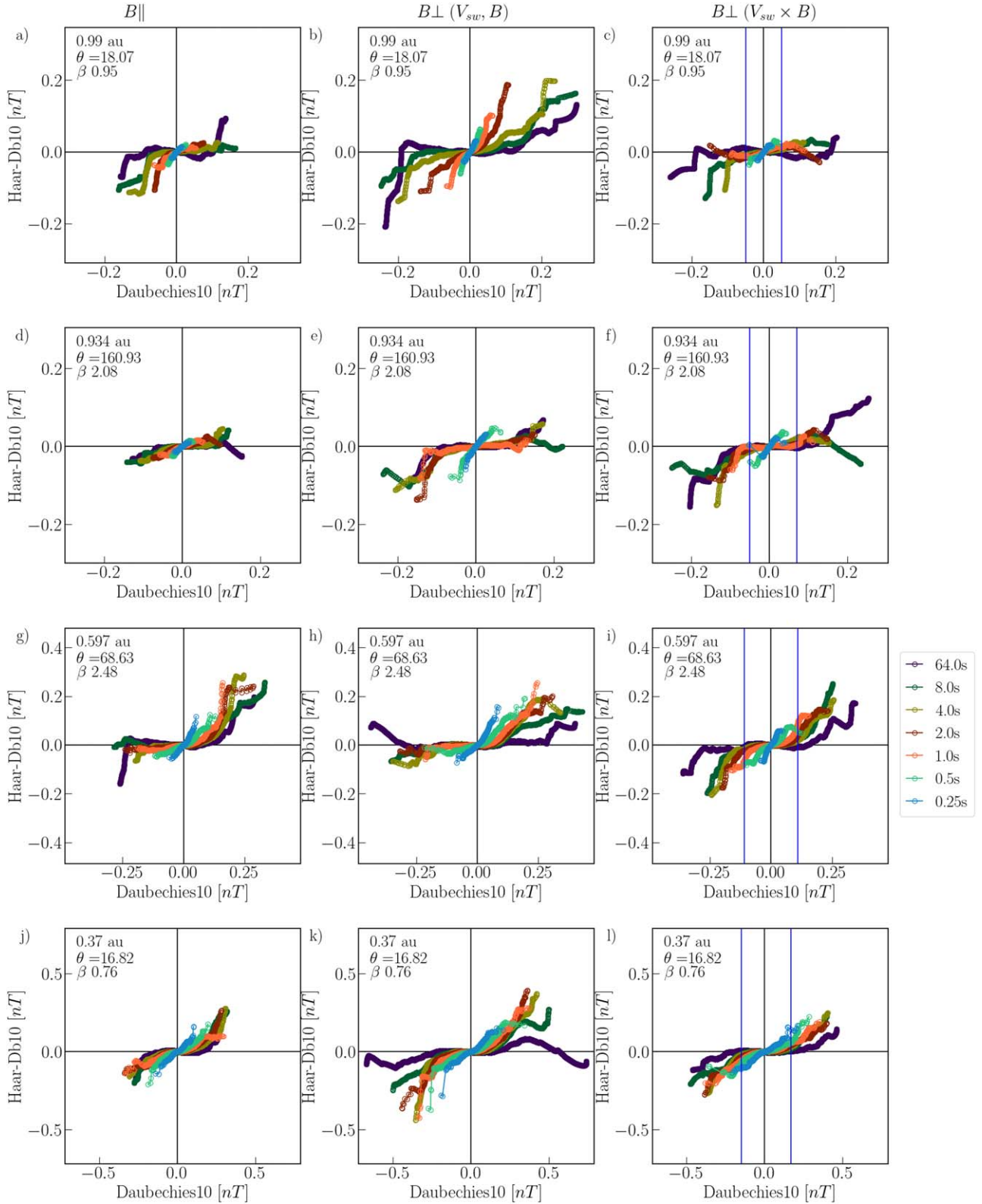


Figure 10. Compensated QQ plots compare the functional forms of the wavelet fluctuation PDFs. The compensated QQ plots are of the $H - Db10$ vs. the $Db10$ wavelet details overplotted per scale for four intervals (rows) and all magnetic field components (columns). From top to bottom the intervals are at 0.9 au, at 0.9 au with $\theta = 160.93$, at 0.597 au and $\beta = 2.48$, and lastly at 0.3 au. The different scales are denoted with different colors, the largest in purple and the smallest in bright blue. Scales from 0.25 to 8 s and additionally 64 s scales are used. If the quantiles lie on the horizontal black line the distributions are the same.

PDFs in the KR are consistent with coherent structure phenomenology. Deep in the inertial range the fluctuation PDFs of both wavelet decompositions coincide, which is consistent

with either coherent structure or wave-packet phenomenology. On intermediate scales where we find a two-component PDF, the coherent structures dominate the PDF tails.

Formally, intermittency is a consequence of multifractality of the time series (Frisch 1995). This corresponds to both non-Gaussian stretched-tail PDFs and a scaling exponent of the structure functions $\zeta(q)$, defined by $S_q(\tau) = \langle |\delta B(\tau, t_j)|^q \rangle \sim \tau^{\zeta(q)}$, which is nonlinearly dependent on q (monotonic curvature; Kiyani et al. 2009, 2006; Frisch 1995). However, the presence of coherent structures does not require multifractality but it does imply non-Gaussian stretched-tail PDFs. In the kinetic range there is mono-scaling; that is, $\zeta(q)$ is linear with q and non-Gaussian stretched-tail PDFs (Kiyani et al. 2009; Frisch 1995). Therefore, a picture of the phenomenology of solar wind turbulence is emerging in which there is multifractal scaling in the inertial range and fluctuations consistent with wave packets, and mono-scaling in the kinetic range and fluctuations consistent with an enhancement of coherent structures. Our results systematically identify a crossover range in which there is a transition from multifractal to monofractal scaling via a two-component fluctuation distribution. Individual event studies based on the Partial Variance Increment have also identified a subrange of the high-frequency IR (Wu et al. 2023).

Additionally, we confirm previously reported results that the IR–KR spectral break typically moves with the larger of the ρ_i and d_i scales depending on distance from the Sun and β (Bruno & Trenchi 2014; Lotz et al. 2023; Šafránková et al. 2023; Chen et al. 2014). The power in all components increases with decreasing distance from the Sun (Chen et al. 2020). We find that in the KR the two wavelet estimates differ, since the Haar wavelet cannot capture exponents steeper than -3 (Farge 1991; Cho & Lazarian 2009).

In this paper we demonstrate how the Haar and Db10 wavelets resolve different underlying physics. Using the Haar and Db10 wavelets, we have detected a crossover from coherent structure phenomenology in the KR to wave-packet phenomenology in the IR. The crossover behavior and range of scales depends on the heliocentric distance and field alignment angle. The population of coherent structures at small scales might suggest an association with the dissipation mechanism of turbulence, as suggested by the enhanced heating signatures found near coherent structures (e.g., Osman et al. 2012b; Sioulas et al. 2022a). A narrower crossover range of scales at large heliocentric distances may be connected to how well the turbulent cascade is developed. The larger range of coherent structure phenomenology at large distances may also be related to the evolution of intermittency with heliocentric distance (e.g., Sioulas et al. 2022b; Bruno et al. 2003; Pagel & Balogh 2003).

This study only included one interval at large θ and one interval at 0.6 au, which thus may only present outliers. A larger number of intervals at large θ as well as intervals at a variety of distances from the Sun should be included in future work. An investigation of the coherent structures and waves present in the respectively dominated scales should give more insight into the physics present and how they connect to each other.

Acknowledgments

All data used in this study are freely available from the following source (accessed last on 2023 October 24): <https://soar.esac.esa.int/soar/>.

Solar Orbiter is a mission of international cooperation between ESA and NASA, operated by ESA.

This work is supported by funding for A.B. from the Science and Technologies Facilities Council (STFC). A.B. also acknowledges support from ISSI. S.C.C. acknowledges support from ISSI via the J. Geiss fellowship and AFOSR grant FA8655-22-1-7056 and STFC grant ST/T000252/1. T.D.d.W. acknowledges support from CNES.

Software: MatLab (The MathWorks Inc. 2022), Scipy (Virtanen et al. 2020), Numpy (version 1.23.0, Harris et al. 2020), Matplotlib (version 3.7.1, Hunter 2007), Astropy (Robitaille et al. 2013; Astropy Collaboration et al. 2018, 2022), Cdfib (Stansby & Harter 2022).

Appendix

A.1. Supporting Methods

A.1.1. Quantile–Quantile Plots

Two distribution functions may differ in their functional form, or in their moments, or in both. This difference can be seen in Quantile–quantile (QQ) plots (Wilk & Gnanadesikan 1968; Easton & McCulloch 1990; Tindale & Chapman 2017). These QQ plots are constructed as follows (also see Wilk & Gnanadesikan 1968; Easton & McCulloch 1990; Tindale & Chapman 2017). The cumulative density function (CDF) $C(x)$ gives the likelihood of observing a value of $X \leq x$ as a function of x . The CDF takes values between zero and 1 and defines the quantiles $x(q)$ of the distribution, so that $C(x(q)) = 0.5$ at the value $x(q)$ where $q = 0.5$, the 0.5 quantile, $C(x(q)) = 0.9$ at the value $x(q)$ where $q = 0.9$, the 0.9 quantile, and so on. The CDF is inverted to give the quantile function $x(q) = C^{-1}(q)$. The QQ plot then compares the quantile functions of a pair of distributions C_1 and C_2 by plotting x_1 versus x_2 with the quantile q as the parametric coordinate. The resulting QQ plot has the values of the quantiles of X on the axes of the two distributions to be compared, and the likelihood q as parametric coordinate. This is illustrated in Figure A1 with two CDFs in panel (a) and a compensated QQ plot in panel (b), where the $x_1 - x_2$ is plotted versus x_2 with the quantiles as parametric coordinate q . With the same functional form, the resulting line of quantiles can take three different shapes. (i) If x_1 and x_2 are drawn from the same distribution, then the compensated QQ plot will be a straight line of $x_2 - x_1 = 0$. (ii) If the distribution has a shift in the mean, then it will be a straight line $x_2 - x_1 = c$ shifted from zero by c . (iii) If there is a change in the variance, then the compensated QQ plot will be a straight line at $x_2 - x_1 = x_1$. If the relationship on the QQ plot is nonlinear, the underlying functional forms of the distributions are different. We use the Statistics and Machine Learning Toolbox from MatLab (The MathWorks Inc. 2022) to determine the quantiles. We find that the wavelet fluctuation PDFs, show three different behaviors illustrated with corresponding compensated QQ plots in Figure A2: (i) the Haar has extended “fatter” tails than the Db10, and the distributions thus differ in σ (panels (a) and (d)); (ii) the distributions are drawn from the same distributions in the core, but diverge in the tails (panels (b) and (e)); and (iii) the distributions are drawn from the same distributions (panels (c) and (f)).

A.2. Supporting Figures

A.2.1. Power Spectral Measures

Figure A3 presents the PSD for all intervals (rows) and each magnetic field component (columns). The increasing power

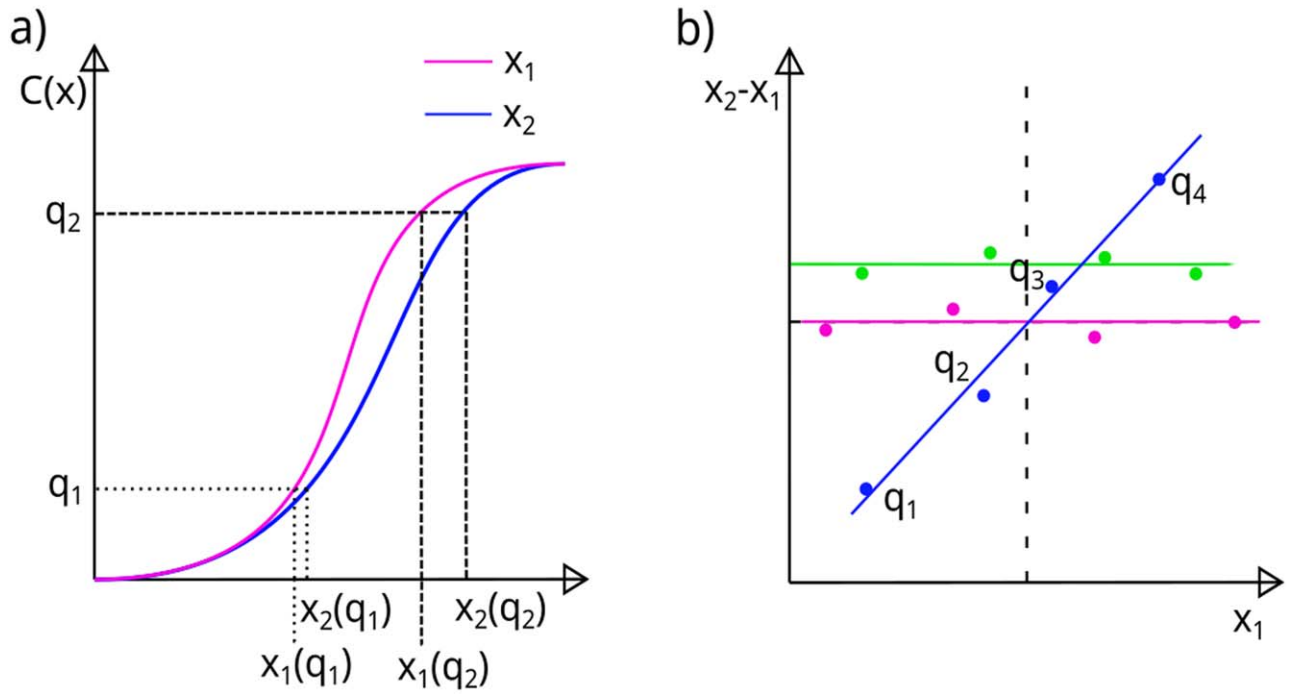


Figure A1. Diagrams showing the construction of the compensated QQ plot. (a) The empirical CDFs of the samples x_1 and x_2 . Proportion q_1 of the data set is bounded by quantile $x_1(q_1)$ in sample x_1 and quantile $x_2(q_1)$ in sample x_2 , similar for q_2 . (b) The compensated QQ plot is produced by plotting $x_1(q)$ against $x_2(q)$ for all values of q . Pink line: $x_2 - x_1 = 0$, i.e., they are the same distribution; green line: $x_2 - x_1 = c$, i.e., different mean; blue line: $x_2 - x_1 = x_1$, i.e., different σ .

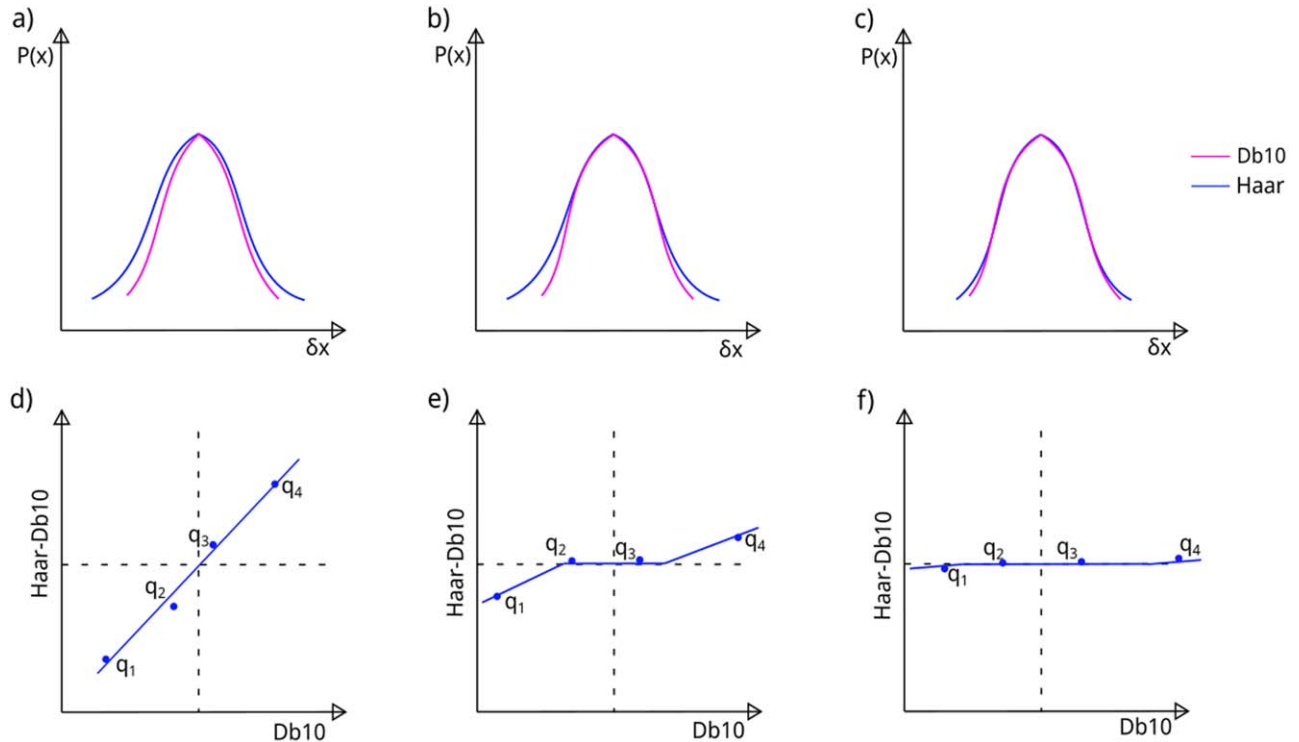


Figure A2. Diagrams showing the construction of the compensated QQ plot. Panels (a)–(c): the PDFs of the samples obtained from Db10 (pink) and Haar (blue) wavelets. Panels (d)–(f): the compensated QQ plot of the above PDF.

levels are seen from top to bottom rows. The movement of d_i and ρ_i is seen clearly as a continuous shift from $\rho_i > d_i$ at 0.9 au to $d_i > \rho_i$ at 0.3 au. With the lower rows the lower KR break scale is seen as well as a smaller $1/f$ range break.

The second moment of the fluctuation PDFs relates to the PSD by definition and is an indicator for the overall power

levels in the fluctuations for each component. Here, we plot the standard deviation σ of the fluctuation PDFs versus temporal scale in Figure A4 for all intervals. As seen in the PSD (Figure 4), the Haar and Db10 wavelets generally agree on the standard deviation in the IR and only significantly diverge at large scales that move toward the upper end of the inertial

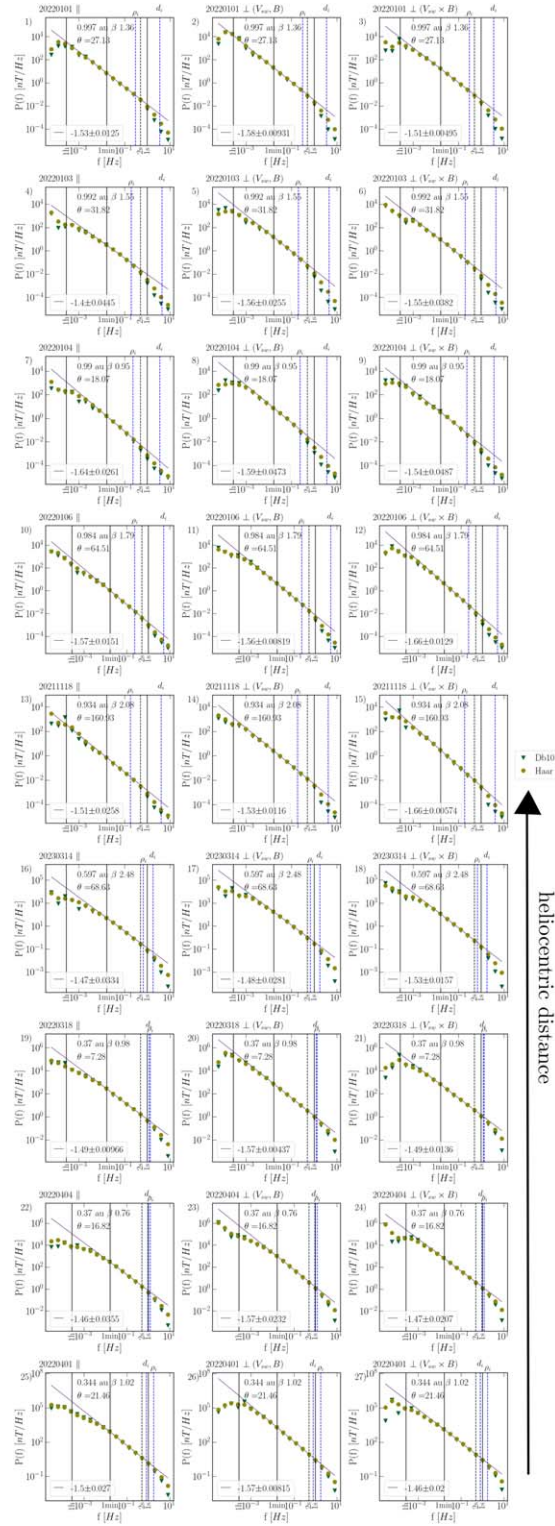


Figure A3. Power spectra of all the different intervals (rows) with decreasing distance from the Sun and for each magnetic field component (columns) and the respective scaling exponent in the inertial range fitted on the Haar wavelet. The 10th order Daubechies wavelet is shown by green triangles, and yellow filled circles are the Haar wavelet. Blue vertical lines denote the ion-gyro frequency ρ_i (dashed) and ion-inertia length d_i (dashed–dotted). Black vertical lines denote scales marked on the x-axis as 1 s, 2 s, 1 minutes, and 1 hr. Purple fit lines to the Haar wavelet power spectra show the spectral exponent, which is quoted to three significant figures.

range. The disagreement in the $1/f$ range is easily seen in the PSD (Figure 4) by an early “roll-off” into the $1/f$ range. In terms of overall power there are three distinct groupings of these intervals. At 0.3 au, the intervals show a progressively

higher σ compared to the intervals at 0.9 au by a factor of ~ 20 at small scales, reducing to ~ 6 at larger scales. The magnetic field component $B_{\perp}(V_{sw}, B)$ has higher σ values than any other component from about 100 s and larger.

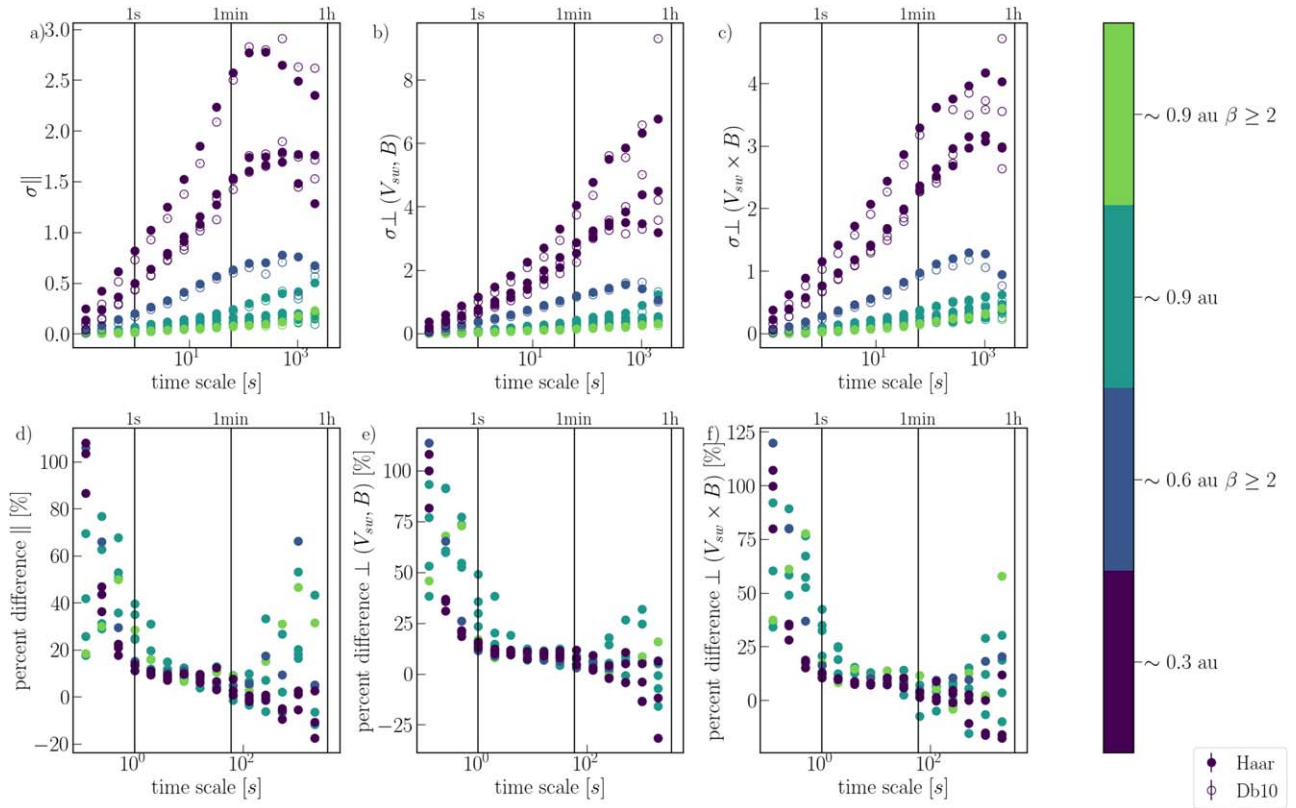


Figure A4. Comparison of standard deviation with increasing timescales for all intervals per magnetic field component. Open circles mark the 10th order Daubechies wavelet, while filled circles are for the Haar wavelet of the corresponding colors per interval. The intervals are divided into four different intervals, with intervals at large distances in lighter colors. An early “roll-off” before the 1 hr scale is observed in σ_{\parallel} , for intervals close to the Sun in $\sigma_{\perp}(V_{sw}, B)$ and for most intervals in $\sigma_{\perp}(V_{sw} \times B)$ in row 1. This is due to the early spectral break to the $1/f$ range in the power spectra. The error bars (too small to be seen) were determined by resampling and the variation of σ values. In row 2, the percentage differences between Haar and Db10 wavelet estimates of σ are presented.

A.2.2. Fluctuation Distributions

The following Figures A5, A6, and A7 show the fluctuation PDF comparison between Haar and Db10 wavelets for each interval (row) across scales from 0.25–8 s to 64 s (columns). The shift of ρ_i (pink circles) and d_i (blue rectangles) is seen, as well as the spectral break in red boxes. The PDFs overlap largely in IR scales and diverge in the tails in KR scales.

Figure A8 provides the compensated QQ plots for all intervals (rows) for each magnetic field component (columns). The gradual alignment of the cores is seen for all intervals and for intervals at 0.9 au a single line with differing σ for KR scales is visible, while intervals at smaller distances show an

initial core in the KR PDFs. The tails are seen to decrease in slope with increasing scales.

A.2.3. Time Series

Figure A9 displays the time-series subintervals and Haar and Db10 wavelet decompositions with corresponding autocorrelation functions (ACFs) for the example interval 2022 January 4 at $\beta = 0.95$ and $\theta = 18^{\circ}07'$ for all magnetic field components. With increasing scale, the fluctuations become more oscillatory and so does the ACF. The Db10 continuously displays a more smooth and oscillatory time series than the Haar wavelet.

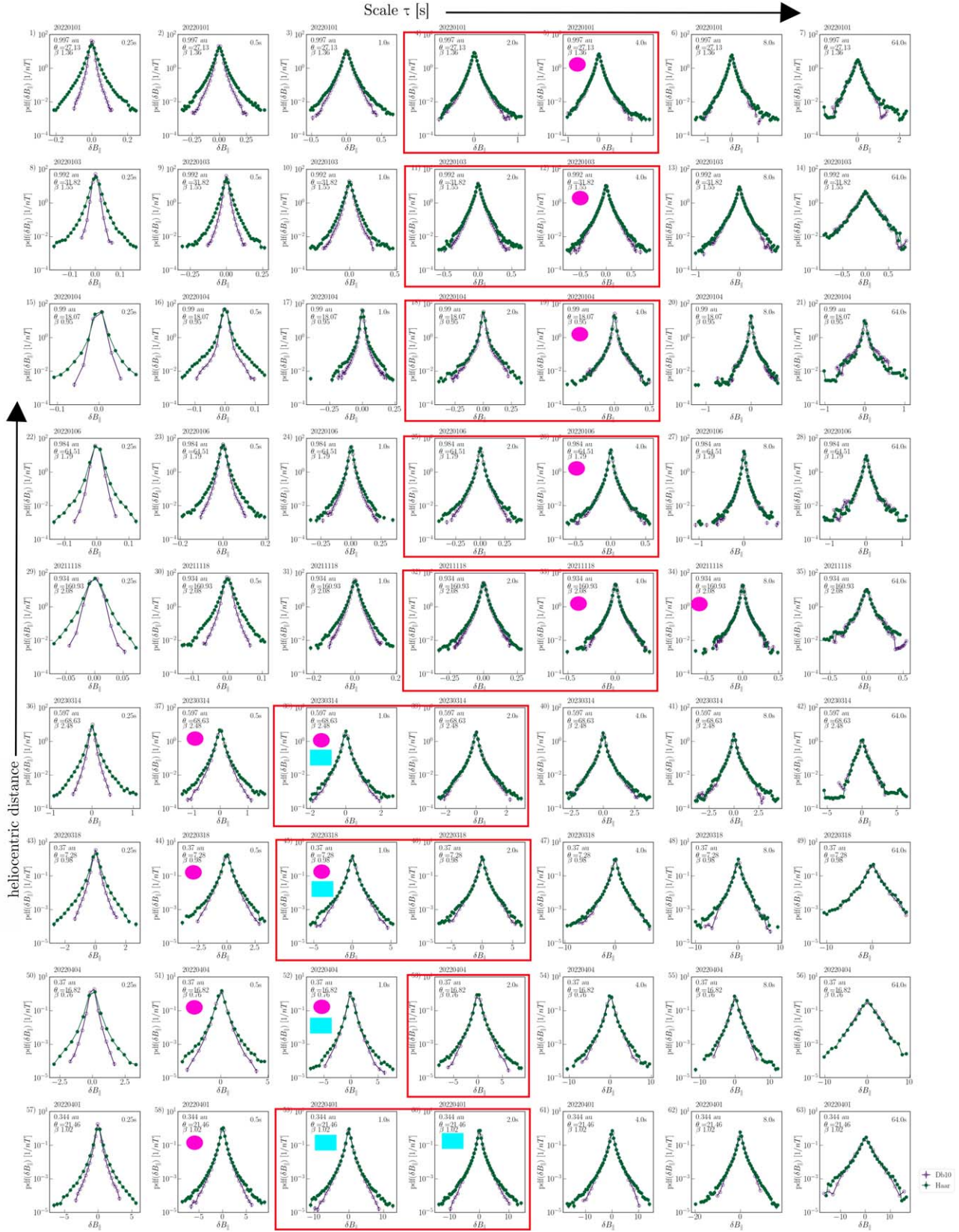


Figure A5. Probability distribution functions of wavelet fluctuations of B_{\parallel} of all intervals in order of decreasing heliocentric distance (top to bottom) and increasing scale (left to right). Filled green circles are obtained from the Haar wavelet, while open purple circles are from the Db10 wavelet. The red boxes mark the spectral break scales. The pink circles denote ρ_i and blue rectangles show d_i (if two panels are marked, the respective characteristic scale is between those two scales). The PDFs are normalized by bin width and overall number of samples of magnetic field data. The number of bins is scaled by the standard deviation σ at the corresponding scale, and bins with fewer than 10 counts are discarded. The error is estimated as \sqrt{n} , where n is the bin count; error bars are too small to be resolved visually.

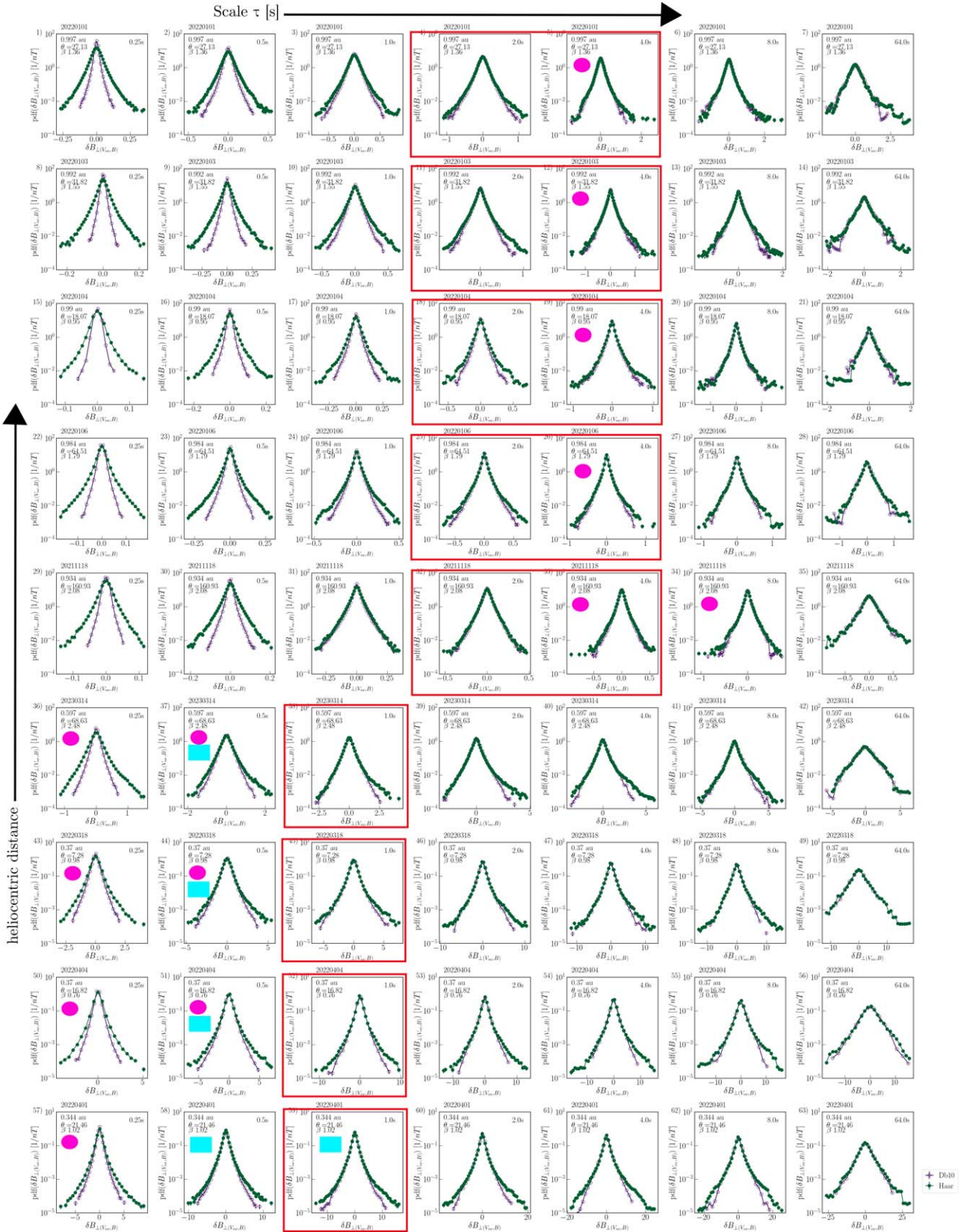


Figure A6. Probability distribution functions of wavelet fluctuations of $B_{l(v_{sw}, B)}$ of all intervals in order of decreasing heliocentric distance (top to bottom) and increasing scale (left to right). Filled green circles are obtained from the Haar wavelet, while open purple circles are from the Db10 wavelet. The red box marks the spectral break scales. The pink circles denote ρ_i and blue rectangles show d_i (if two panels are marked, the respective characteristic scale is between those two scales). The PDFs are normalized by bin width and overall number of samples of magnetic field data. The number of bins is scaled by the standard deviation σ at the corresponding scale, and bins with fewer than 10 counts are discarded. The error is estimated as \sqrt{n} , where n is the bin count; error bars are too small to be resolved visually.

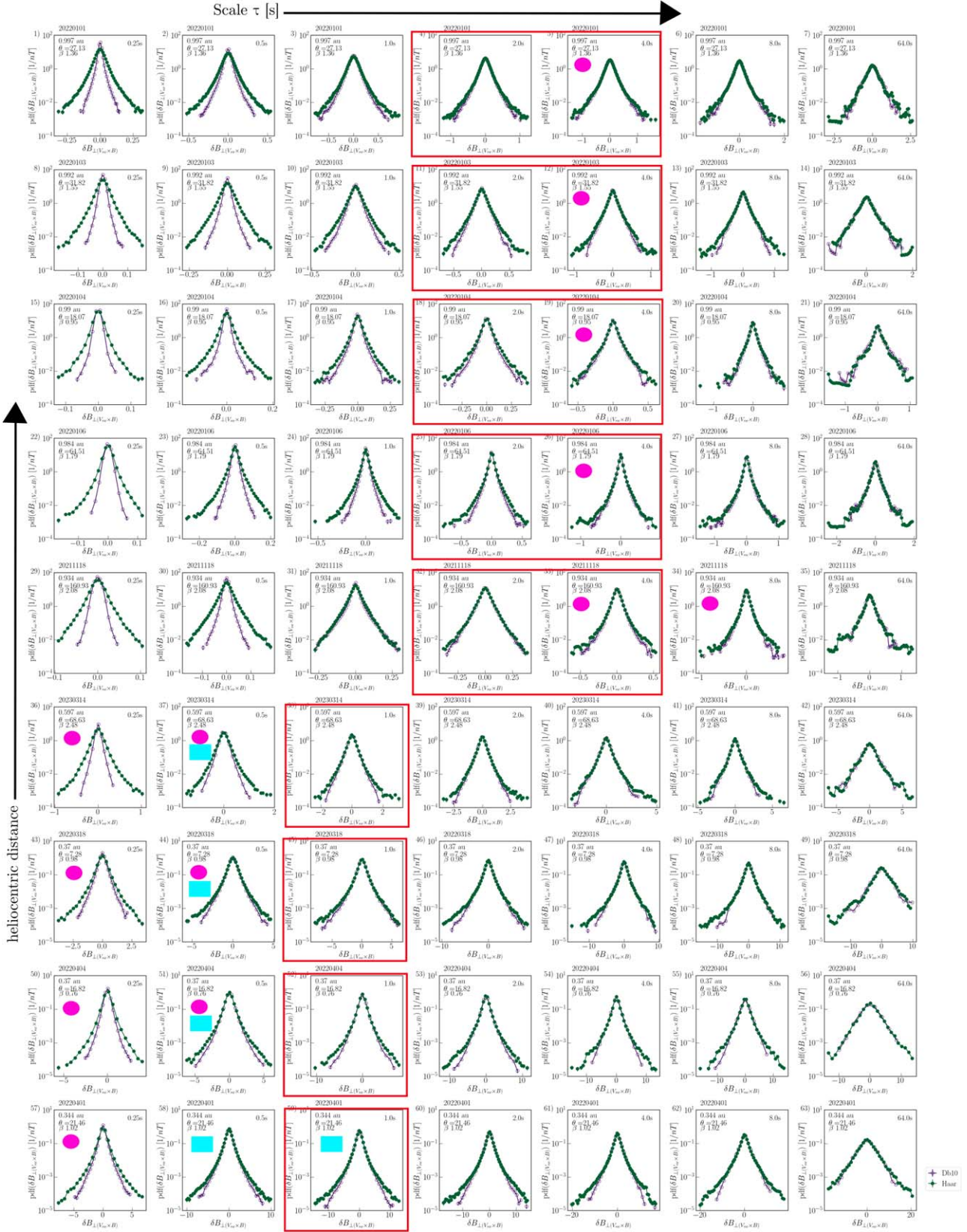


Figure A7. Probability distribution functions of wavelet fluctuations of $B_{\perp}(V_{sw} \times B)$ of all intervals in order of decreasing heliocentric distance (top to bottom) and increasing scale (left to right). Filled green circles are obtained from the Haar wavelet, while open purple circles are from the Db10 wavelet. The red box marks the spectral break scales. The pink circles denote ρ_i and blue rectangles show d_i (if two panels are marked, the respective characteristic scale is between those two scales). The PDFs are normalized by bin width and overall number of samples of magnetic field data. The number of bins is scaled by the standard deviation σ at the corresponding scale, and bins with fewer than 10 counts are discarded. The error is estimated as \sqrt{n} , where n is the bin count; error bars are too small to be resolved visually.

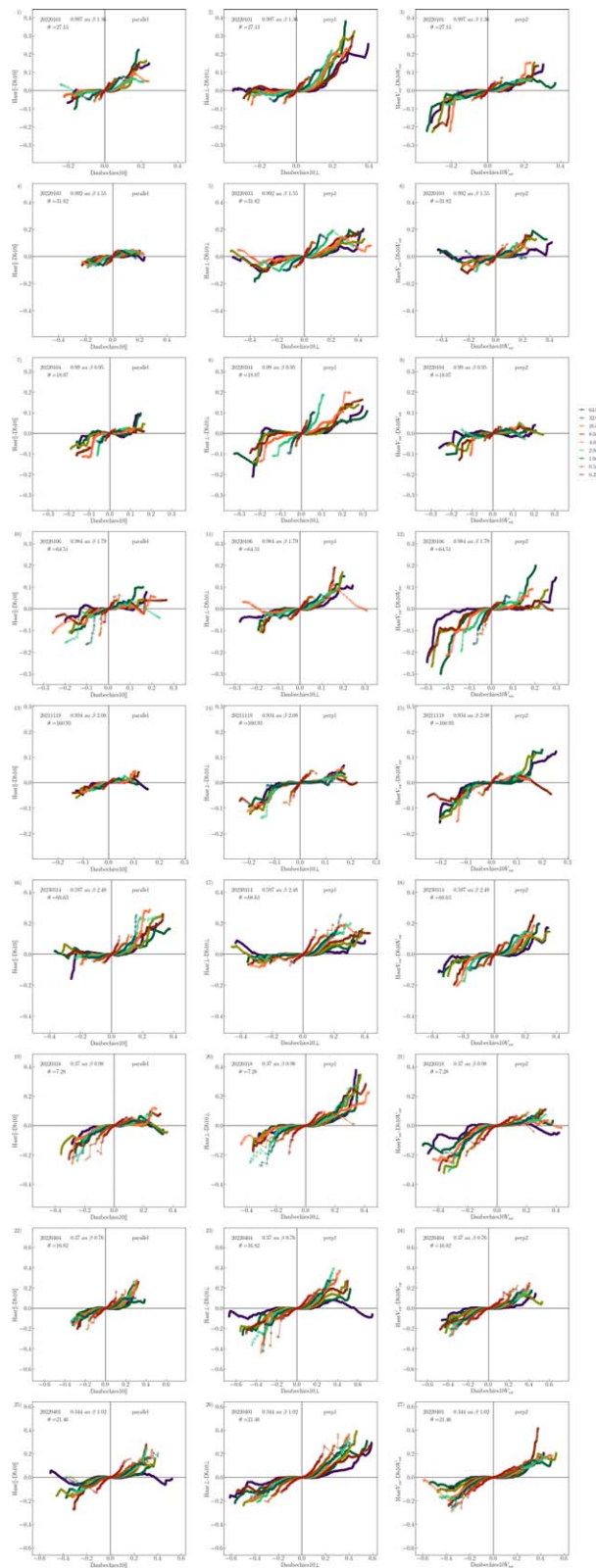


Figure A8. QQ plots of the Haar wavelet details vs. the 10th order Daubechies wavelet details overlaid per scale for all intervals (rows, also labeled at the top-right corner of the panels) and all magnetic field components (columns). The different scales are denoted with different colors. Scales from 0.25 to 4 s and additionally 64 s scales are used. The fluctuations are normalized to the magnitude.

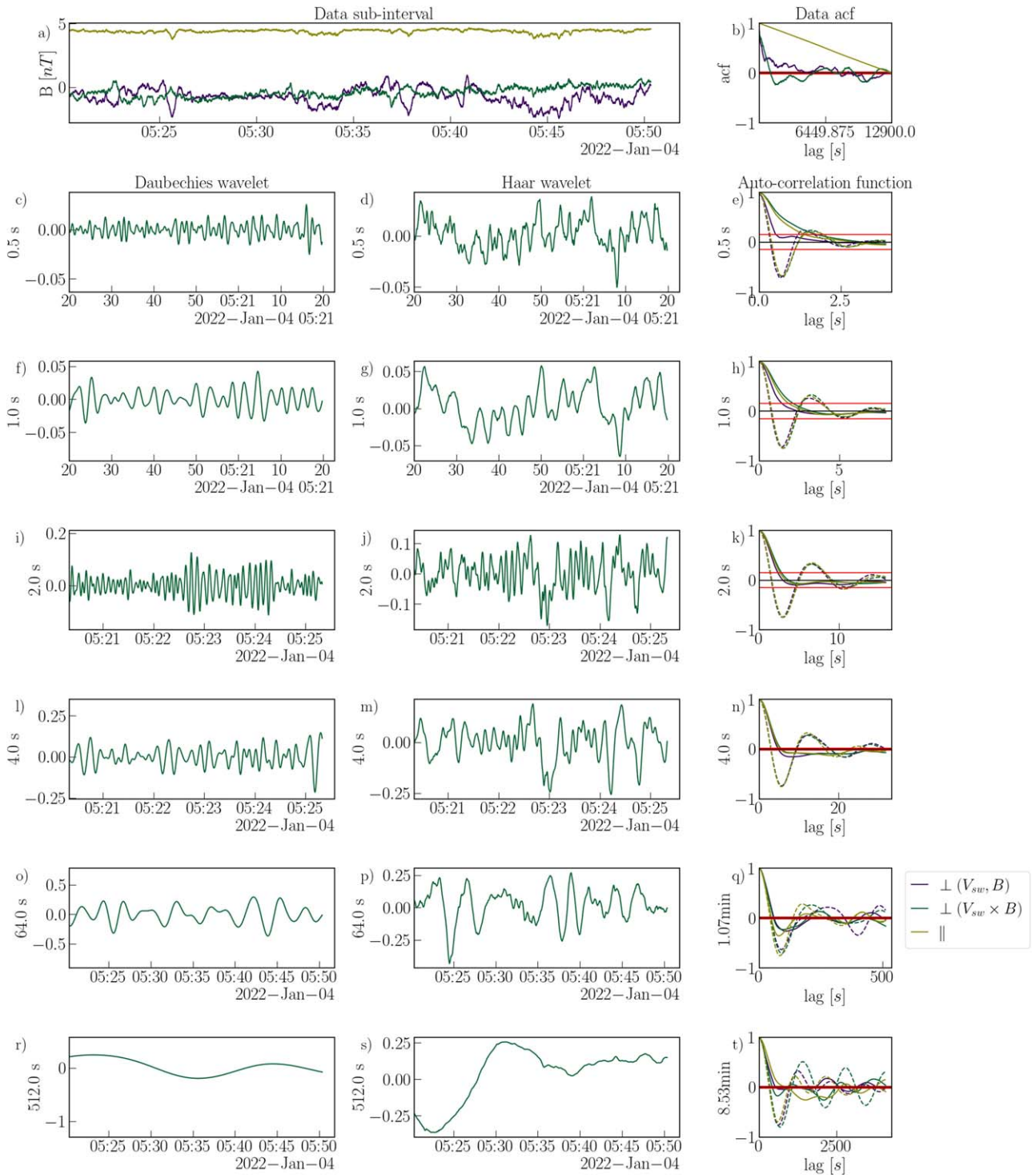


Figure A9. Decomposition of magnetic field time series of interval at 0.989 au from 2022 January 4 on scales 0.5 to 4 s and 64 s and 512 s of time series (left) by Db10 and (middle) by Haar wavelets. Right panels show ACFs of the middle third of decomposition time series of Db10 (dashed lines) and Haar (continuous lines). Red horizontal lines indicate the significance level obtained from autocorrelations of colored noise with corresponding spectral exponents in the kinetic and inertial range. In purple the $B_{\perp(V_{sw}, B)}$, in green the $B_{\perp(V_{sw} \times B)}$, and finally in yellow B_{\parallel} .

ORCID iDs

Alina Bendt <https://orcid.org/0009-0002-6513-5689>
 Sandra Chapman <https://orcid.org/0000-0003-0053-1584>
 Thierry Dudok de Wit <https://orcid.org/0000-0002-4401-0943>

References

Alexandrova, O., Carbone, V., Veltri, P., & Sorriso-Valvo, L. 2008, *ApJ*, 674, 1153
 Alexandrova, O., Chen, C. H. K., Sorriso-Valvo, L., Horbury, T. S., & Bale, S. D. 2013, *SSRv*, 178, 101
 Astropy Collaboration, Price-Whelan, A. M., Lim, P. L., et al. 2022, *ApJ*, 935, 167

- Astropy Collaboration, Price-Whelan, A. M., Sipőcz, B. M., et al. 2018, *AJ*, **156**, 123
- Bandyopadhyay, R., & McComas, D. J. 2021, *ApJ*, **923**, 193
- Bavassano, B., Dobrowolny, M., Fanfoni, G., Mariani, F., & Ness, N. F. 1982, *SoPh*, **78**, 373
- Beresnyak, A. 2012, *MNRAS*, **422**, 3495
- Bolzán, M. J. A., Guarnieri, F. L., & Vieira, P. C. 2009, *BrJPh*, **39**, 12
- Bourouaie, S., Alexandrova, O., Marsch, E., & Maksimovic, M. 2012, *ApJ*, **749**, 102
- Bruno, R. 2019, *E&SS*, **6**, 656
- Bruno, R., & Carbone, V. 2013, *LRSP*, **10**, 2
- Bruno, R., Carbone, V., Primavera, L., et al. 2004, *AnGeo*, **22**, 3751
- Bruno, R., Carbone, V., Sorriso-Valvo, L., & Bavassano, B. 2003, *JGRA*, **108**, 1130
- Bruno, R., & Trenchi, L. 2014, *ApJL*, **787**, L24
- Camussi, R., & Guj, G. 1997, *JFM*, **348**, 177
- Chapman, S. C., & Hnat, B. 2007, *GeoRL*, **34**, L17103
- Chen, C. H. K. 2016, *JPIPh*, **82**, 535820602
- Chen, C. H. K., Leung, L., Boldyrev, S., Maruca, B. A., & Bale, S. D. 2014, *GRL*, **41**, 8081
- Chen, C. H. K., Mallet, A., Yousef, T. A., Schekochihin, A. A., & Horbury, T. S. 2011, *MNRAS*, **415**, 3219
- Chen, C. H. K., Bale, S. D., Bonnell, J. W., et al. 2020, *ApJS*, **246**, 53
- Chhiber, R., Matthaeus, W. H., Bowen, T. A., & Bale, S. D. 2021, *ApJL*, **911**, L7
- Cho, J., & Lazarian, A. 2009, *ApJ*, **701**, 236
- Cuesta, M. E., Parashar, T. N., Chhiber, R., & Matthaeus, W. H. 2022, *ApJS*, **259**, 23
- Daubechies, I. 1990, *ITIT*, **36**, 961
- Daubechies, I. 1992, in Conf. on Wavelets, Ten Lectures on Wavelets (Philadelphia, PA: Society for Industrial and Applied Mathematics)
- Do-Khac, M., Basdevant, C., Perrier, V., & Dang-Tran, K. 1994, *PhyD*, **76**, 252
- Duan, D., He, J., Bowen, T. A., et al. 2021, *ApJL*, **915**, L8
- Easton, G. S., & McCulloch, R. E. 1990, *J. Am. Stat. Assoc.*, **85**, 376
- Farge, M. 1991, *PhFLA*, **3**, 2029
- Farge, M. 1992, *AnFRM*, **24**, 395
- Farge, M., Kevlahan, N., Perrier, V., & Goirand, E. 1996, in Proc. IEEE 84, Wavelets and Turbulence, 639
- Frisch, U. 1995, Turbulence: The Legacy of A.N. Kolmogorov (Cambridge: Cambridge Univ. Press)
- Gomes, L. F., Gomes, T. F. P., Rempel, E. L., & Gama, S. 2023, *MNRAS*, **519**, 3623
- Greco, A., Matthaeus, W. H., Perri, S., et al. 2017, *SSRv*, **214**, 1
- Harris, C. R., Millman, K. J., van der Walt, S. J., et al. 2020, *Natur*, **585**, 357
- He, J., Tu, C., Marsch, E., & Yao, S. 2012, *ApJ*, **745**, L8
- Hess-Nielsen, N., & Wickerhauser, M. 1996, in Proc. IEEE 84, Wavelets and Time-frequency Analysis, 523
- Hnat, B., Chapman, S. C., & Rowlands, G. 2003, *PhRvE*, **67**, 056404
- Horbury, T. S., Forman, M. A., & Oughton, S. 2008, *PhRvL*, **101**, 175005
- Horbury, T. S., O'Brien, H., Blazquez, I. C., et al. 2020, *A&A*, **642**, A9
- Hunter, J. D. 2007, *CSE*, **9**, 90
- Iroshnikov, P. S. 1963, *AZh*, **40**, 742
- Katul, G., Vidakovic, B., & Albertson, J. 2001, *PhFI*, **13**, 241
- Kiyani, K., Chapman, S. C., & Hnat, B. 2006, *PhRvE*, **74**, 051122
- Kiyani, K., Osman, K., & Chapman, S. 2015, *RSPSA*, **373**
- Kiyani, K. H., Chapman, S. C., Khotyaintsev, Y. V., Dunlop, M. W., & Sahraoui, F. 2009, *PhRvL*, **103**, 075006
- Kiyani, K. H., Chapman, S. C., Sahraoui, F., et al. 2013, *ApJ*, **763**, 10
- Koga, D., Chian, A. C.-L., Miranda, R. A., & Rempel, E. L. 2007, *PhRvE*, **75**, 046401
- Kolmogorov, A. N. 1991, *RSPSA*, **434**, 9
- Lotz, S., Nel, A. E., Wicks, R. T., et al. 2023, *ApJ*, **942**, 93
- Lovejoy, S., & Schertzer, D. 2012, *NPGEO*, **19**, 513
- Mallat, S. 1989, *ITPAM*, **11**, 674
- Marino, R., & Sorriso-Valvo, L. 2023, *PhR*, **1006**, 1
- Markovskii, S. A., Vasquez, B. J., & Smith, C. W. 2008, *ApJ*, **675**, 1576
- Maruca, B. A., Qudsi, R. A., Alterman, B. L., et al. 2023, *A&A*, **675**, A196
- Matthaeus, W., Goldstein, M. L., & Roberts, D. A. 1990, *JGR*, **95**, 20673
- Matthaeus, W. H., & Goldstein, M. L. 1982, *JGR*, **87**, 6011
- Meneveau, C. 1991, *JFM*, **232**, 469
- Müller, D., Marsden, R. G., St. Cyr, O. C., Gilbert, H. R. & The Solar Orbiter Team 2013, *SoPh*, **285**, 25
- Müller, D., Cyr, O. C. S., Zouganelis, I., et al. 2020, *A&A*, **642**, A1
- Narasimha, R. 2007, *Sadha*, **32**, 29
- Nickolas, P. 2017, Wavelets: A Student Guide (Cambridge: Cambridge Univ. Press),
- Nicol, R. M., Chapman, S. C., & Dendy, R. O. 2008, *ApJ*, **679**, 862
- Osman, K., Matthaeus, W., Gosling, J., et al. 2014, *PhRvL*, **112**, 215002
- Osman, K. T., Matthaeus, W. H., Hnat, B., & Chapman, S. C. 2012a, *PhRvL*, **108**, 261103
- Osman, K. T., Matthaeus, W. H., Wan, M., & Rappazzo, A. F. 2012b, *PhRvL*, **108**, 261102
- Oughton, S., Matthaeus, W. H., Wan, M., & Osman, K. T. 2015, *RSPTA*, **373**, 20140152
- Owen, C. J., Bruno, R., Livi, S., et al. 2020, *A&A*, **642**, A16
- Pagel, C., & Balogh, A. 2003, *JGRA*, **108**, 1012
- Percival, D. B., & Walden, A. T. 2000, Wavelet Methods for Time Series Analysis (Cambridge: Cambridge Univ. Press),
- Perri, S., Goldstein, M. L., Dorelli, J. C., & Sahraoui, F. 2012, *PhRvL*, **109**, 191101
- Podesta, J. J. 2009, *ApJ*, **698**, 986
- Podesta, J. J., Roberts, D. A., & Goldstein, M. L. 2007, *ApJ*, **664**, 543
- Roberts, D. A. 1990, *JGR*, **95**, 1087
- Roberts, O., Alexandrova, O., Kajdič, P., et al. 2017, *ApJ*, **850**, 120
- Robitaille, T. P., Tollerud, E. J., Greenfield, P., et al. 2013, *A&A*, **558**, A33
- Sahraoui, F., Goldstein, M. L., Robert, P., & Khotyaintsev, Y. V. 2009, *PhRvL*, **102**, 231102
- Salem, C. S., Howes, G. G., Sundkvist, D., et al. 2012, *ApJL*, **745**, L9
- Schneider, K., & Farge, M. 2001, in Wavelet Transforms and Time-Frequency Signal Analysis., ed. L. Debnath (Cambridge, MA: Birkhäuser Boston), 181
- Sioulas, N., Huang, Z., Velli, M., et al. 2022b, *ApJ*, **934**, 143
- Sioulas, N., Velli, M., Chhiber, R., et al. 2022a, *ApJ*, **927**, 140
- Sorriso-Valvo, L., Carbone, V., Veltri, P., Consolini, G., & Bruno, R. 1999, *GeoRL*, **26**, 1801
- Stansby, D., & Harter, B. 2022, MAVENSDC/cdfib; Zenodo, doi:10.5281/zenodo.7011489
- Šafránková, J., Němeček, Z., Němec, F., et al. 2023, *ApJL*, **946**, L44
- Tessein, J. A., Smith, C. W., MacBride, B. T., et al. 2009, *ApJ*, **692**, 684
- The MathWorks Inc., 2022 Wavelet Toolbox v6.2, (R2022b) Update 2, <https://www.mathworks.com>
- Tindale, E., & Chapman, S. C. 2017, *JGRA*, **122**, 9824
- Torrence, C., & Compo, G. P. 1998, *BAMS*, **79**, 61
- Tu, C. Y., & Marsch, E. 1995, *SSRv*, **73**, 1
- Tu, C.-Y., Pu, Z.-Y., & Wei, F.-S. 1984, *JGR*, **89**, 9695
- Turner, A. J., Gogoberidze, G., & Chapman, S. C. 2012, *PhRvL*, **108**, 085001
- Veltri, P. 1999, *PPCF*, **41**, A787
- Verscharen, D., Klein, K. G., & Maruca, B. A. 2019, *LRSP*, **16**, 5
- Virtanen, P., Gommers, R., Oliphant, T. E., et al. 2020, *NatMe*, **17**, 261
- Wang, X., Chapman, S. C., Dendy, R. O., & Hnat, B. 2023, *A&A*, **678**, A186
- Wang, X., Tu, C.-Y., He, J.-S., & Wang, L.-H. 2018, *JGRA*, **123**, 68
- Welch, P. 1967, *IEEE Trans. Audio Electroacoust.*, **15**, 70
- Wicks, R. T., Horbury, T. S., Chen, C. H. K., & Schekochihin, A. A. 2010, *MNRAS*, **407**, L31
- Wilk, M. B., & Gnanadesikan, R. 1968, *Biometrika*, **55**, 1
- Wu, H., Huang, S., Wang, X., et al. 2023, *ApJL*, **947**, L22
- Wu, P., Perri, S., Osman, K., et al. 2013, *ApJL*, **763**, L30
- Yamada, M., & Ohkitani, K. 1991a, *FIDyR*, **8**, 101
- Yamada, M., & Ohkitani, K. 1991b, *PhPh*, **86**, 799
- Yordanova, E., Balogh, A., Noullez, A., & von Steiger, R. 2009, *JGRA*, **114**, A08101
- Zhang, J., Huang, S. Y., He, J. S., et al. 2022, *ApJL*, **924**, L21
- Zhou, M., Liu, Z., & Loureiro, N. F. 2023, *PNAS*, **120**, e2220927120